学位論文

Mid Infrared Studies of Massive Star Formation (中間赤外線を用いた大質量星形成の研究)

平成26年12月博士(理学)申請

東京大学大学院理学系研究科
天文学専攻

内山 瑞穂

Abstract

Massive stars, with masses larger than $8M_{\odot}$, are ones of the most important sources for dynamical and chemical evolutions in the universe. In spite of the importance of the massive stars, their formation processes have not been well understood. One of the most serious problems is that massive clouds are gravitationally unstable in early collapsing phases. The thermal Jeans masses in infrared dark clouds (IRDCs), considered as their parental dense clouds, are estimated as about 1 $M_{\odot}$. This implies that the mass is too small to make a massive core and eventually a massive star. Certain mechanisms producing additional inner pressure to overcome a self-gravity of a massive collapsing cloud (CC) in the IRDC are required. One of the possible mechanisms to produce the additional pressure is heating of the gas, which increases thermal pressure of the gas. For example, the gas with a temperature of higher than 40 K can physically support the massive CC with a mass enough to form a massive star against the self-gravity. Among various heating sources, radiation by young stellar objects (YSOs) in the IRDC is considered as a promising one because it could serve as a universal source without invoking any external objects.

We focused on the highest mass YSO in the IRDC because it most effectively heats the IRDC due to its largest luminosity among the YSOs in the IRDC. According to simple estimation, the radiation by a higher intermediate-mass YSO (HIYSO; defined as a YSO with a mass of 5 *to* 7 $M_{\odot}$ in this work) is required to heat the gas with a mass of 8 $M_{\odot}$ up to 40 K in total. When the HIYSO already exists before the formation of the massive CC in the IRDC, the radiation by the HIYSO would heat the gas sufficiently. This means that the massive young stellar object (MYSO) is expected to be generally accompanied by the older HIYSO within 0.1-pc region, corresponding to the heating area of the HIYSO radiation. However, it has not been observationally confirmed. To examine whether the star formation sequence between the HIYSO and the MYSO within 0.1-pc size region has been consistent with our expectation or not, information of an age and a mass of individual object is strongly desired.

In this work, three massive star forming regions, the M8E, the RAFGL 6366S, and the IRAS 18317-0513 regions, have been observed in the mid-infrared wavelengths, including 31- and 37-micron bands, to examine the star formation sequences between HIYSOs and MYSOs. Our developed mid-infrared camera MAX38 mounted on the miniTAO telescope has been used for this study. The observations have brought us the first images of these regions at longer than 30-microns from ground. The spatial resolution in our observations achieves approximately 8 arcsec at 31 microns and 9 arcsec at 37 microns which is the highest resolution among the other observations carried out so far. Images of all these 0.1-pc size regions, which have achieved enough high spatial resolution to resolve individual objects, have been successfully obtained. These images have enabled us to measure an infrared luminosity of each object separately.

Individual spectral type and stellar mass have been estimated from the derived luminosities using a stellar model. In the M8E and RAFGL 6366S regions, it has been found that the objects associated with the UCHII regions have relatively lower masses than the other objects. Because

less massive YSOs are expected to have longer star formation timescales, they may form earlier and more massive objects latter. These star formation sequences have also been confirmed by a quantitative age estimation of each object. Furthermore, a literature survey has been carried out to extend the number of samples. The similar star formation sequence has also been found in one region out of three. In total, such star formation sequences have been confirmed in three out of six regions and the same star formation sequences could have not been ruled out in the other three regions. This suggests that the radiative heating by the previously formed HIYSO helps the formation of MYSO in the massive star forming regions.

Furthermore, we have estimated the gas temperature and the mass of the CC in the heated gas using a simple cloud model under assumption of dust thermal equilibrium. It has been suggested that the radiative heating by the HIYSO can increase the gas temperature enough to form the MYSO in a certain case within a possible range of a luminosity and a temperature of the HIYSO. It has also been suggested that the increased mass of the CC, assuming that it is equal to the Jeans mass, from the radiative heating by the HIYSO almost corresponds to the mass of the MYSO in a certain case.

This work may provide the first observational evidence that the radiative heating by the previously formed HIYSO induces the formation of the MYSO. This result also suggests speculation that masses of newly formed YSOs in the IRDCs always increase from the first-formed low-mass YSOs to finally-formed MYSOs due to the radiative heating by the previously formed YSOs in the IRDCs. Detailed theoretical models of the radiative heating in the IRDCs and our planning future large survey will give further information of the star formation sequences between HIYSOs and MYSOs and the effect of the radiative heating by the HIYSO. They may also reveal the universality of such star formation sequences with more extended mass ranges including intermediate mass objects.

Contents

Chapter 1

Introduction

1.1 Importance of massive stars

Massive stars, with masses larger than $8M_{\odot}$, are ones of the most important sources for dynamical and chemical evolutions in the universe. They provide strong UV photons to surrounding interstellar medium (ISM) and form ionized regions. They also supply strong mechanical energy to the ISM via fast stellar winds, outflows, and supernova explosions (Zinnecker and Yorke 2007). The supernova explosions are also important to generate interstellar magnetic fields by accelerating cosmic rays via shock fronts (Zinnecker and Yorke 2007). The massive stars are main suppliers of heavy elements, heavier than helium, and have a great influence on evolution of the early universe (Zinnecker and Yorke 2007). The heavy elements formed at a center of the massive star spread to the interstellar space widely and enrich the interstellar environments through supernova explosion at the end of the life. The heavy elements increase an efficiency of gas cooling as well as being main components of dust grain and large molecules (Zinnecker and Yorke 2007). The dust and the molecules including the heavy elements are essential matters for forming rocky planets like the Earth and eventually birth of living organisms like a humankind.

1.2 Overview of massive star formation

In spite of the importance of the massive stars, their formation processes have not been well understood. The primary reason is the fact that a massive star forming region is affected by strong extinction in most wavelengths. Since the massive stars quickly evolve, they are deeply embedded in gas and dust clouds especially during their forming periods. Another reason is the fact that these stars are located distant from us because of their rareness as compared with lower-mass stars. This makes it difficult to resolve each forming massive star.

The massive stars are considered to form in relatively dense clouds called infrared dark clouds (IRDCs) with typical densities of $n_{H_2} \sim 10^4 cm^{-3}$, sizes of about 1 to 10 pc, and temperatures of about 10 K (Tan et al. 2014; Longmore et al. 2011) as illustrated in Figure 1.1. A part of the IRDC, called a massive collapsing cloud (a massive CC) in this paper, collapses into a dense core with a typical size of approximately 0.1 pc (Churchwell 2002; Tan et al. 2014). The center of the massive core is still cold, about 10 to 20 K, and millimeter continuum emission is mainly detected from there (Churchwell 2002). Then, a part of the massive core collapses and makes a massive young stellar object (MYSO) surrounded by an optically thick circumstellar-envelope (Tan et al. 2014). Since the dust envelope is heated up to typically about 100 K by radiation from the MYSO, the observed flux is dominated by thermal re-emission from the envelope (Grave and Kumar 2009; Sridharan et al. 2002). In this evolutional phase, the parental massive core is

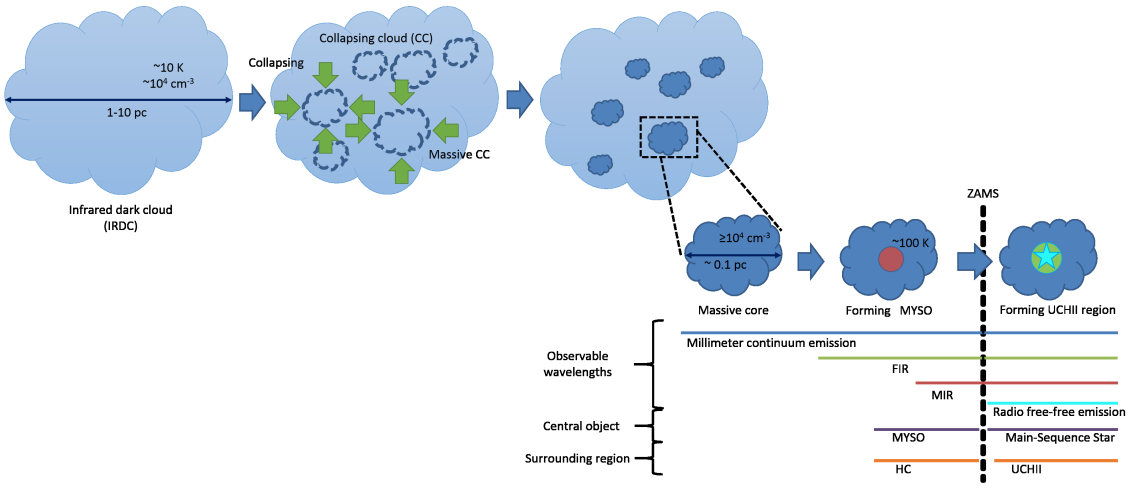

Figure 1.1: Overview of massive star formation from the IRDC to the main-sequence stages. Evolutional sequence of a massive star after forming a massive core is magnified. Observable wavelengths at each evolutional stage are also represented.

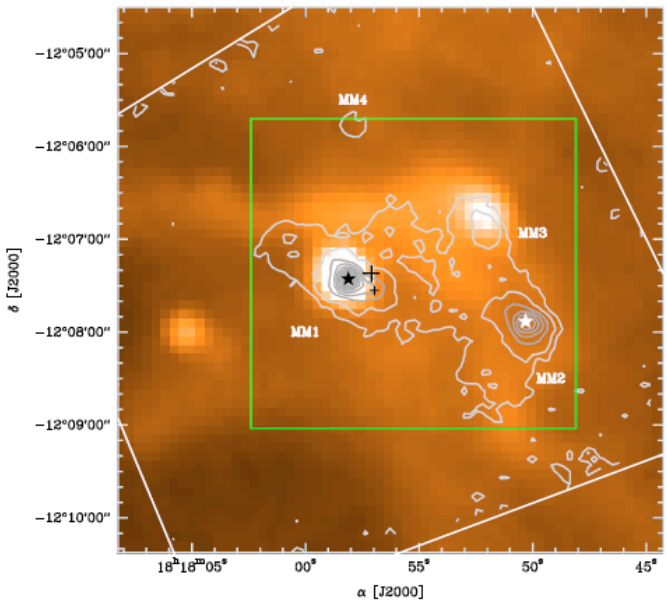

Figure 1.2: Typical hot cores with MYSOs, the IRAS 18151-1208 region (Marseille et al. 2008). Color scale represents the 8 micron map by the MSX satellite. White and gray contours represent the 1.2-mm map obtained with the IRAM 30m telescope/MAMBO.

also heated by the MYSO and observed as a hot core (HC) (Churchwell 2002). The HC usually shows large optical-depths of molecular-lines in the radio wavelengths and this suggests that the massive core includes a dense, $n_{H_2} \geq 10^7 cm^{-3}$, region where the MYSO should be located (Churchwell 2002). Observational examples of the HCs are shown in Figure 1.2. Three bright sources, MM1, MM2, and MM3 are detected with millimeter continuum in the IRAS 18151-1208 region. While the MIR emission is detected from MM1 and MM3, it is not from MM2. These differences are considered to be caused by different evolutional stages of the central objects (Marseille et al. 2008).

The MYSO starts emitting ionizing photons from when reaching around the zero age main-sequence (ZAMS) stage (Hosokawa and Omukai 2009). In the early main-sequence stage, mass accretion prevents an ionizing region around the central star from expanding because most ionizing photons are absorbed by accreting dust and gas (Churchwell 2002). When the mass accretion stops or sufficiently decreases, the ionized region grows up and forms an ultra compact HII region (UCHII region), defined as a dense, $n_e \gtrsim 10^4 cm^{-3}$, and compact, size $\lesssim 10^{17} cm$, HII region (Churchwell 2002). To make and sustain the UCHII region, a luminous central star with a spectral type as early as B3 is needed at least. While the UCHII region is still embedded in the gas and dust in the massive core, an existence and characteristics of the UCHII region can be examined by free-free emission in the centimeter wavelengths. A typical observed case of an object with an UCHII region is shown in Figure 1.3. The lifetime of the UCHII region is observationally estimated to be as short as $10^5 yr$ (Churchwell 2002). Therefore, the massive stars accompanied by the UCHII regions are considered to be after but at near the ZAMS stage. The UCHII regions are considered to keep expanding and then be observed as compact HII regions with a typical size of 0.05 to 0.4 pc (Mezger et al. 1967) and eventually HII regions with a typical size of larger than 10 pc (Phillips 2008).

1.3 Core formation and fragmentation problem

As described above, an evolutionary sequence of the massive star in the formation stage has been revealed by the previous observational and theoretical works. However, a serious problem has remained in an early forming stage of the massive core. A molecular cloud is supported by thermal gas-pressure against self-gravity. The mass of the molecular cloud determined by the physical balance is known as the thermal Jeans mass and proportional to $T_{gas}^{3/2} \rho_{gas}^{-1/2}$, where T_{gas} and ρ_{gas} are a temperature and a density of the gas in the molecular cloud, respectively. The molecular cloud with a mass larger than the Jeans mass is physically unstable and eventually fragments into small-mass clouds. The Jeans mass is estimated as about 1 $M_\odot$ under physical conditions of a typical IRDC, density of about $10^4 cm^{-3}$ and a temperature of about 10 K, assuming isothermal and uniform-density gas. This implies that the massive CC, which eventually produces a massive core and a massive star, cannot exist in the typical IRDC. This is a fundamental problem in the massive star formation. Another problem that a massive core fragments to multiple low-mass objects during its collapsing phase also exists, called as the core fragmentation problem (Tan et al. 2014). Both problems are serious for the massive star formation. In this study, the former problem of the massive CC in the IRDCs, which is more fundamental one, is focused on.

To physically support the massive CC, some mechanisms providing additional pressure to overcome a self-gravity of the massive CC are required. One possible mechanism is strong internal turbulence. Actually, observations have shown that the IRDCs are usually in turbulent condition with a line width of approximately 1 $km\ s^{-1}$ (Tan et al. 2014). This would be strong enough to provide the sufficient pressure. However, the strength of the turbulence is different

by location and a number of stagnation points of the turbulence co-exist in the IRDC. Since the pressure around the stagnation points is relatively weak, the gas is expected to form only the low-mass cores around them. This expectation has been supported by Padoan and Nordlund (2002) and Mac Low and Klessen (2004). They have carried out numerical and analytical calculations about the turbulent cloud and suggested that the turbulence is not effective for increasing the Jeans mass in the IRDC due to the stagnation points.

Magnetic field can also produce the additional pressure in the IRDC (Tan et al. 2014). For example, the magnetic field with a strength of 0.03 mG can physically support the massive CC with a mass of 8 $M_{\odot}$ (Draine 2011). On the other hand, typical strength of the magnetic fields in IRDCs has not been accurately measured so far (Tan et al. 2014). Recently, Crutcher et al. (2010) and Crutcher (2012) have found the relation between the gas density and the median strength of the magnetic field with a wide gas density range of $100 \lesssim n_{H_2} \lesssim 10^7\ cm^{-3}$ and suggested that the strength of the magnetic field in a typical IRDC with a density of $n_{H_2} \sim 10^4\ cm^{-3}$ would be 0.05 mG. This seems to be strong enough, but it is noteworthy that it is not derived by measurements but by an interpolation. Direct measuring the strength of the magnetic fields in IRDCs is physically difficult due to lack of suitable molecular line tracers for cold and dense IRDCs (Tan et al. 2014). Therefore, the magnetic field may contribute to support the massive CCs in the IRDCs but the practical effect of this mechanism is not clear.

Gas heating increases the thermal pressure in IRDCs. If the gas temperature is heated up to 40 K, a CC with a mass of 8 $M_{\odot}$ can be sufficiently supported. External shock and external radiation from a nearby supernova or an expanding HII region are possible heating sources. Actually, Beuther et al. (2012) have demonstrated that some star-less molecular clouds in the W43 complex are heated up to 20-30 K by the external radiation from nearby massive stars. However, all the massive CCs would not be commonly heated up sufficiently by the external shock and the external radiation. The other possible source is radiation from previously formed young stellar objects (YSOs) in the IRDC. This heating source is considered as a promising one because it could serve as a universal source without invoking any external objects as mentioned above.

1.4 Radiative heating feedback by previously formed YSOs

The luminosity of a YSO strongly depends on its mass and a more massive YSO is much more luminous through the pre-main sequence stage (Siess et al. 2000; Palla and Stahler 1993; Hosokawa and Omukai 2009). It is presumed that the total luminosity of a cluster of YSOs is dominated by the luminosity of the highest mass YSO among them. Therefore, the highest mass YSO previously formed in the IRDC should be focused on as a heating source. According to a simple estimation, the gas temperature of 40 K can be achieved if a higher intermediate-mass YSO (HIYSO; defined as a YSO earlier than about B3 with a mass of 5 *to* 7 $M_{\odot}$ in this work) exists in the IRDC. In other words, the formation of the MYSO may be induced by the radiative heating by a slightly less massive object. Based on the analogy of the radiative heating by the HIYSO, the following star formation scenario is speculated: In a primitive IRDC, only low-mass YSOs formed at first. These stars effectively heat up the cloud and a higher mass YSO forms from the heated gas. The higher mass YSO is more luminous and more effectively heats up the gas and the mass of a newly formed star gradually increases. Eventually, a HIYSO and subsequently a MYSO forms. We call this as "mass-sequential star formation". Figure 1.4 shows a schematic drawing of this scenario.

When the mass-sequential star formation occurs in the IRDC, the MYSO is expected to be generally accompanied by the older HIYSO within a 0.1-pc region, corresponding to a heating

area of the HIYSO radiation (Scoville and Kwan 1976). However, the star formation sequence between the HIYSO and the MYSO in such a small region has not been well studied before. In order to study the star formation sequence, the information of an age and a mass of each object is required.

In general, the age of a YSO or a star is difficult to be estimated. However, for massive objects including HIYSOs and MYSOs, it is easily distinguished whether the object already reaches at the ZAMS stage or not by existence of an UCHI region. Radio interferometers are powerful tool to detect the free-free emission from the UCHII regions with high spatial resolution of less than 5 arcsec.

The masses of the HIYSOs and the MYSOs are estimated from their bolometric luminosities. As mentioned in section 1.2, the apparent effective temperatures of the HIYSOs and the MYSOs are about 100K and the peak wavelength of the spectral energy distributions (SEDs) is located in the long-MIR, defined as longer than $25\mu m$ in this work (Grave and Kumar 2009; Churchwell 2002; Sridharan et al. 2002). For accurate estimation of the bolometric luminosity, the long-MIR is particularly important (Figure 1.5). Furthermore, high spatial resolution is important to resolve multiple sources including the HIYSOs and the MYSOs in complex regions and measure their fluxes separately. For example, spatial resolution of 10 arcsec is needed to resolve two objects with a separation of 0.1 pc at a distance of 1 kpc. Since most of the massive star forming regions are located further than 1 kpc [1], higher spatial resolution is required. However, such a high spatial resolution has not been achieved in the long-MIR wavelengths so far.

Radiation in the long-MIR wavelengths have been normally observed by space telescopes. However, space telescopes lunched so far are not useful for studying massive star forming regions in detail. Their apertures are not so large and the spatial resolution limited by the diffraction of the apertures is slightly insufficient. In addition, observations of nearby massive star forming regions frequently suffer a saturation problem. Ground-based telescopes with large apertures achieve high spatial resolutions in the MIR, but they cannot access the long-MIR wavelengths due to atmospheric extinction even in the Mauna Kea site with an altitude of 4,200 meters.

1.5 Scope of this work

This work concentrates on revealing the star formation sequences between the HIYSOs and the MYSOs in a couple of massive star forming regions with a size of about 0.1 pc. To exclude the effects of the heating by the external shocks and external radiation, massive star forming regions without structure indicating the dynamical and the radiative interaction are selected as observational targets.

To achieve sufficient spatial resolution in the long-MIR, new observations have been carried out with a new mid-infrared instrument optimized for the long-MIR observations, Mid-infrared Astronomical eXplorer 38(MAX38; Nakamura et al. 2010 and Asano et al. 2012), mounted on a ground-based telescope, The University of Tokyo Atacama 1.0-m Telescope (miniTAO; Minezaki et al. 2010). The miniTAO is located on the summit of Co. Chajnantor at Atacama desert in Chile, the altitude of which is 5,640 meters, and this site is the only place that enables us to carry out stable observations in the long-MIR wavelengths up to 38 um (Miyata et al. 2012). To maximize the advantages of the site, the MAX38 has a wavelength coverage up to 38 micron and an imaging capability with a high spatial resolution, less than 10 arcsec (Nakamura et al. 2010;

[1] There are a few extremely nearby massive star forming regions such as the Orion BN/KL massive star forming region. In these regions, it has been suggested that severe dynamical interaction would have happen in the past (De Buizer et al. 2012) and they do not seem to be suitable for examining only the effect of the radiative heating.

Asano et al. 2012). We have observed totally three massive star forming regions and successfully obtained spatially resolved new images in the long-MIR in this work.

Details of target selection and observational status are represented in Chapter 2. The results of the observations including photometry and luminosity estimation are described in Chapter 3. The mass of each YSO and the star formation sequence between a HISYO and a MYSO in each observed region are discussed in Chapter 4. The literature survey is also described in Chapter 4. The quantitative evaluation of the effect of the radiative heating by the HIYSO is described in Chapter 5. Finally, the conclusion and the future plan are shown in Chapter 6.

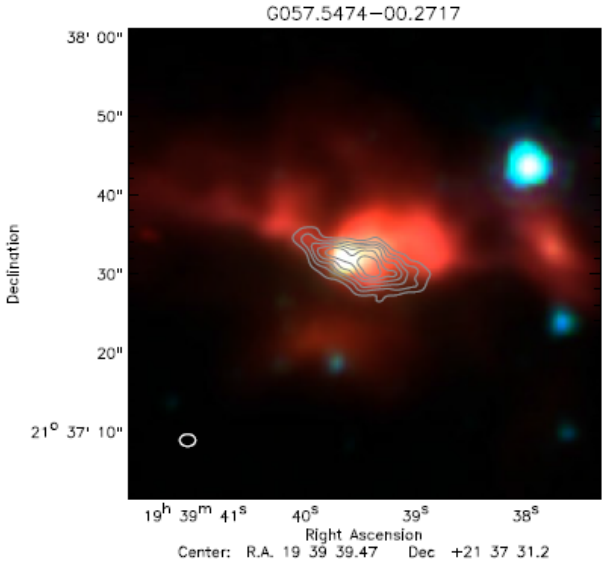

Figure 1.3: Typical image of UCHII region, G057.5474-00.2717 (Urquhart et al. 2009). Three color maps are from the GLIMPSE infrared survey with the Spitzer/IRAC. White contours represent observations of the free-free emission in 6 cm wavelengths by the VLA.

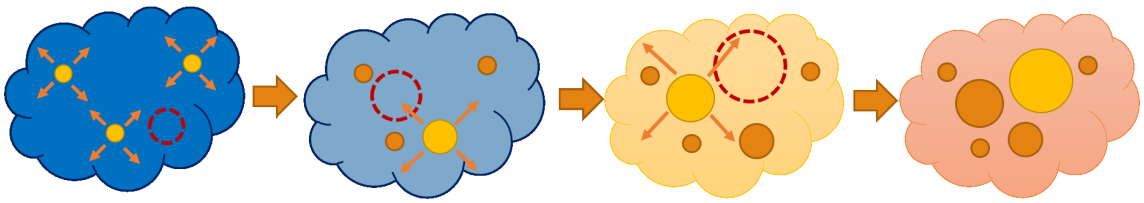

Figure 1.4: The sketch of the mass-sequential star formation in the IRDC. The highest mass YSO at a certain point helps the formation of more massive YSO.

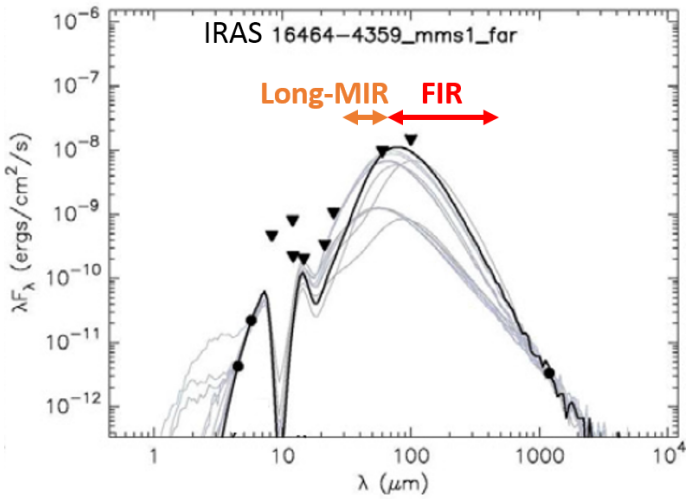

Figure 1.5: Typical SED of MYSO, IRAS 16464-4539 (Grave and Kumar 2009). Dots and triangles represent observed fluxes and upper limits due to low resolution, respectively. Bold and thin lines show fitting results of SED. A peak of radiation energy is located from the long-MIR to the FIR wavelength range.

Chapter 2

Observations

2.1 miniTAO/MAX38

Mid-infrared observations of massive star forming regions have been carried out with the miniTAO/MAX38, which are parts of the University of Tokyo Atacama Observatory Project (PI: Yuzuru Yoshii; Yoshii et al. 2010). The MAX38 has a 128 × 128 Si:Sb BIB detector with a pixel scale of 1.26 arcsec. It has a field of view of 2 × 2.5 $arcmin^2$ for imaging observations (the remaining 0.5 × 2.5 $arcmin^2$ of the detector array is used for spectroscopy). The detailed performance of the MAX38 is reported by Asano et al. (2012). The profiles of filters used in this work are listed in Table 2.1. The MAX38 has achieved diffraction-limited high spatial resolution of approximately 8 and 9 arcsec at 31 and 37 microns, respectively.

2.1.1 Condition of observations

Observations have been conducted in September in 2010, May in 2011, November in 2011, and October in 2012 under good weather conditions with a precipitable water vapor (PWV) of from 0.35 to 1.05 millimeters as listed in Tables 2.3 and 2.4.

Observations have been conducted with standard chopping and nodding. Chopping frequency has been 3 Hz on September 20 2010 and 2 Hz in the other observations , respectively. Chopping throw has been adopted as 20, 32, and 38 arcsec to prevent the overlap of the images. Chopping directions have been both north-south and east-west in November in 2011 and only north-south in the other observations. Nodding frequency has been 0.05 Hz on September 20 in 2010 and 0.02 Hz in the other observations, respectively. Nodding throw has been adopted as 30, 35, and 40 arcsec and nodding directions have been orthogonal to the chopping directions. All four images of the chopping and nodding beams have been on the detector (on-chip chop and nod method).

2.2 Observation Targets

Based on following criteria, we have selected massive star forming regions as observation targets.

- Containing multiple candidates of HIYSOs, MYSOs, or objects with UCHII regions within a few × 0.1 pc-size area reported in the RMS project (Lumsden et al. 2013), which is the most recent large survey of massive star forming regions in multi-wavelengths including NIR imaging archive (2MASS), NIR spectroscopy (Cooper et al. 2013), MIR imaging archive (GLIMPSE and MIPSGAL), MIR imaging (mainly MSX and Michelle (Lumsden

et al. 2013)), sub-mm imaging archive (ATLASGAL), millimeter spectroscopy (Urquhart et al. 2008a), and centimeter interferometric imaging (VLA and ATCA (Urquhart et al. 2009)) (Note that not all above observational data is available for all regions), or by de Wit et al. (2009), which is the recent survey observations with high spatial resolution (less than 1 arcsec) in the MIR especially including 24.5 μm images.

- Observed in multi-wavelengths including at least infrared and centimeter wavelengths to evaluate the possibility of observations in the long-MIR and to determine the evolutional stage.
- Containing multiple IR or radio objects with separations of larger than about 4 arcsec to resolve each object spatially with the miniTAO/MAX38 in the long-MIR.
- Containing the only objects that do not accompany bright nebulae in the MIR to derive luminosities accurately.
- Flux of a region at 30 μm is estimated as more than 100 Jy. This flux threshold is set to detect the second or third luminous object which has about 10 % of a total flux in the region, corresponding to achieving signal-to-noise ratio of approximately 10 with roughly 1000 seconds integration using miniTAO/MAX38 with 31 μm filter.

Selected ten massive star forming regions are listed in Table 2.2. Four massive star forming regions among the ten selected regions have been observed with the miniTAO/MAX38. However, image data of the IRAS 06063+2040 region is not used for the following analysis because this data has not been obtained with the sufficient signal to noise ratio to detect multiple components. In the other three regions, the M8E, the RAFGL 6366S, and the IRAS 18317-0513 region, observations have been achieved sufficient signal-to-noise ratios. All the three regions have been studied in multi-wavelengths by previous works but the long-MIR imagings with high spatial resolution have been lacking until now. Their coordinates, observing date, filters in use, integration time, and PWV and airmass at the observing time are listed in Table 2.3.

Table 2.1: MAX38's Filter Parameter

Filter	λ [μm]	$\Delta\lambda$ [μm]	spatial resolution
8.9μm	8.9	0.8	2.5"
12μm	12.2	0.5	2.5"
18μm	18.7	0.9	4.6"
25μm	24.5	1.9	6.3"
31μm	31.7	2.2	7.8"
37μm	37.3	2.4	9.2"

Table 2.2: The selected targets list

Name	R.A. [1] (J2000)	Dec [1] (J2000)	Distance	Observation status
RAFGL 6366S	$06^h\ 08^m\ 41\overset{s}{.}0$	$+21^\circ\ 31'\ 01''$	2.0 kpc [2]	observed & detected
IRAS 06063+2040	$06^h\ 09^m\ 21\overset{s}{.}9$	$+20^\circ\ 39'\ 28''$	2.0 kpc [3]	observed & not detected
IRAS 09230-5148	$09^h\ 24^m\ 41\overset{s}{.}2$	$-52^\circ\ 01'\ 54''$	5.7 kpc	not observed
IRAS 13395-6153	$13^h\ 43^m\ 02\overset{s}{.}1$	$-62^\circ\ 08'\ 52''$	5.3 kpc	not observed
IRAS 16362-4845	$16^h\ 40^m\ 00\overset{s}{.}1$	$-48^\circ\ 51'\ 45''$	2.0 kpc	not observed
IRAS 16533-4009	$16^h\ 56^m\ 47\overset{s}{.}8$	$-40^\circ\ 14'\ 25''$	2.4 kpc [4]	not observed
IRAS 16533-4009	$17^h\ 02^m\ 08\overset{s}{.}4$	$-41^\circ\ 46'\ 53''$	4.7 kpc	not observed
IRAS 17016-4124	$17^h\ 05^m\ 09\overset{s}{.}8$	$-41^\circ\ 29'\ 04''$	2.8 kpc	not observed
M8E	$18^h\ 04^m\ 53\overset{s}{.}2$	$-24^\circ\ 26'\ 42''$	1.5 kpc [5]	observed & detected
IRAS 18317-0513	$18^h\ 34^m\ 25\overset{s}{.}6$	$-05^\circ\ 10'\ 50''$	3.0 kpc	observed & detected

Distances without footnote symbols are from Urquhart et al. (2008a)
[1]http://simbad.u-strasbg.fr/simbad/
[2]Klein et al. (2005)
[3]Kawamura et al. (1998)
[4]Moisés et al. (2011)
[5]Simon et al. (1984)

Table 2.3: The observed targets list and the conditions of miniTAO/MAX38 Observations

Object	R.A. [1] (J2000)	Dec [1] (J2000)	Date	Filter	Int.time (sec)	PWV (mm) [2]	Airmass	Chopping
M8E	$18^{h}\ 04^{m}\ 53\overset{s}{.}2$	$-24^{\circ}\ 26'\ 42''$	2010/9/20	31μm	1100	0.60	1.08	32”
				18μm	100	0.60	1.18	
			2011/5/27	37μm	4000	0.45	1.03	38”
				25μm	1000	0.50	1.27	
RAFGL 6366S	$06^{h}\ 08^{m}\ 41\overset{s}{.}0$	$21^{\circ}\ 31'\ 01''$	2011/10/31	31μm	1000	0.85	1.41	20”
				18μm	500	0.85	1.40	
				12μm	500	0.85	1.48	
			2011/11/01	8.9μm	200	0.85	1.50	20”
			2012/10/24	25μm	1600	0.40	1.52	38”
				37μm	1600	0.45	1.41	
IRAS 18317-0513	$18^{h}\ 34^{m}\ 25\overset{s}{.}6$	$-05^{\circ}\ 10'\ 50''$	2011/11/04	31μm	1500	0.35	1.06	20”
				18μm	600	0.35	1.07	
				12μm	1000	0.35	1.05	

[1] http://simbad.u-strasbg.fr/simbad/

[2] PWV values were obtained from APEX weather data archive (http://www.apex-telescope.org/weather/) and modified to the values of observing site using the method shown in Miyata et al. (2012)

2.2.1 M8E

The M8E region is a massive star forming region located at an almost south-east edge of the famous M8, known as the Lagoon nebula (Tothill et al. 2002). The low spatial-resolution, about 30 arcsec, mapping surveys with sub-millimeter dust continuum and molecular line emission around the M8E region have represented that a separation between a neighbor core is approximately 3 arcmin (Tothill et al. 2002), corresponding to as large as 1 pc, as shown in Figure 2.1. In addition, obtained images have shown that the M8E region has a central-concentrated morphology of dust and gas density structure and does not have a tail-like structure. Therefore, it is suggested that the M8E region does not suffer from external interaction from the neighbor.

Its distance is 1.25-1.5 kpc (Arias et al. 2007; Simon et al. 1984) assuming that its distance is the same as that of the M8 derived by photometric and spectroscopic observations. In this work, 1.5 kpc is adopted as is often the case with the previous works, such as Linz et al. (2009). The M8E region consists of two close objects (Simon et al. 1984). Their projected separation is about 7 arcsec and it corresponds to $10^4 AU$ as shown in Figure 2.2. The one object, called M8E-IR in Simon et al. (1984), is an Orion-BN like MYSO without radio free-free emission. Although M8E-IR is faint at the optical wavelengths, it is very bright at the near-infrared and longer wavelengths. The other object, named M8E-radio (Simon et al. 1984), has an UCHII region detected in the centimeter wavelengths (Simon et al. 1984; Molinari et al. 1998). M8E-radio itself have been also detected in the MIR wavelengths (de Wit et al. 2009; Linz et al. 2009). Electron density of the UCHII region accompanied with M8E-radio is approximately $10^5 cm^{-3}$ and its size is about 600 AU, corresponding to 10^{16} cm (Simon et al. 1984), which are typical values of UCHII regions (density $\gtrsim 10^4 cm^{-3}$ and size $\lesssim 10^{17} cm$) (Churchwell 2002).

2.2.2 RAFGL 6366S

The RAFGL 6366S region is a massive star forming region and considered as a part of the Gemini OB1 molecular complex. It is located at about 10 arcmin, corresponding to approximately 6 pc, south-east from the S247 HII region (Rodon 2009; Carpenter et al. 1995). Global dense gas distribution of the RAFGL 6366S region has not shown tail-like structure obtained by observations in millimeter molecular line emission with low spatial resolution, about 45 arcsec, in the studies of Carpenter et al. (1995) and Klein et al. (2005) as shown in Figure 2.3. In addition, although the RAFGL 6366S region is next to the S247 HII region, the large-scale kinematic temperature distribution derived from observations by Carpenter et al. (1995) has represented an almost flat temperature distribution of approximately 10 K around 2 pc-scale from the RAFGL 6366S region. These results have suggested that the RAFGL 6366S region is not externally interacted by the S247 HII region or any external sources.

The distance towards the RAFGL 6366S region is 2.0 kpc although it has large uncertainty up to ±50% because this is a kinematic distance of molecular gas (Klein et al. 2005). The RAFGL 6366S region consists of several stars and protostars. A spatially resolved image of millimeter dust continuum emission using the radio-interferometer obtained by Rodon (2009) has shown that this region has elongated structure from north-east to south-west as shown in Figure 2.4. There are an object with an UCHII region in the north-east part of this region (Kurtz et al. 1994), a MYSO in the central part, and an infrared-quiet (dark) region in the south-west part. The separation between the object with the UCHII region and the MYSO is approximately 7.1 arcsec, which corresponds to $1.4 \times 10^4 AU$. Kurtz et al. (1994) have reported that the detected UCHII region has a relatively high electron density of $> 0.6 \times 10^4 cm^{-3}$ and a relatively small size of $<$ 1200 AU ($< 2 \times 10^{16} cm$). Observations with the MSX satellite have shown that the most of mid-infrared fluxes come from near the MYSO. SiO outflow is associated

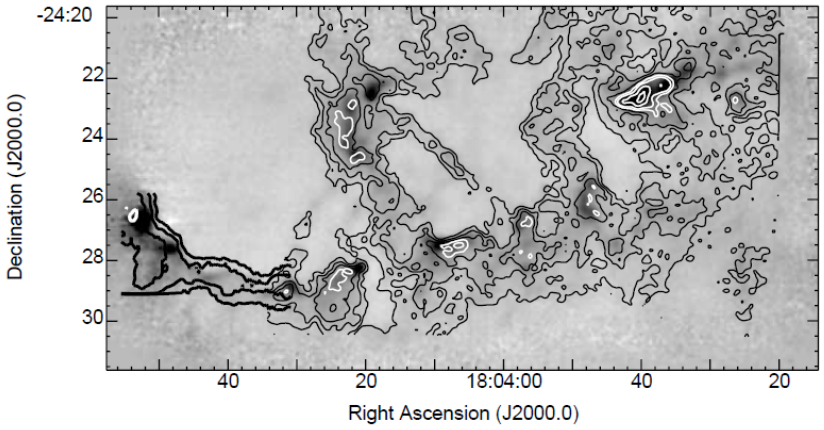

Figure 2.1: The image of the south-east part of the M8 nebula from the observations of Tothill et al. (2002). Gray scale map represents 850 micron dust emission. The M8E region corresponds to a big black spot at an east edge in this map. Thick contours represent at values of $^{12}CO(2-1)$ integrated intensity of 25, 50, 100 $Kkms^{-1}$ (black) and 150 $Kkms^{-1}$ (white).

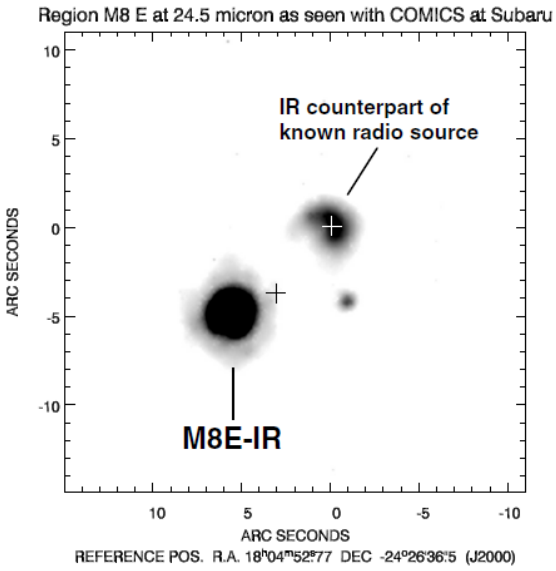

Figure 2.2: The image of the M8E region at 24.5 micron from the Linz et al. (2009). Gray scale map represents 24.5 micron dust emission. The white plus mark represent the position of M8E-radio detected in centimeter wavelengths.

with the MYSO and this object seems to be young and massive object (Rodon 2009). There is also a near-infrared object in the central part of the region. It is 2 arcsec apart from the MYSO and thought as a low-mass YSO (Rodon 2009). These two objects in the central part have been clearly resolved by observations at 11.2 μm with high spatial resolution using the Gemini-North/Michelle (Urquhart et al. 2008b).

2.2.3 IRAS 18317-0513

The IRAS 18317-0513 is known as a bright massive star forming region in the infrared wavelengths (Faúndez et al. 2004). It is suggested that the IRAS 18317-0513 region is not affected by any external sources because the relatively low spatial-resolution, 12 to 25 arcsec, mapping observations with millimeter dust continuum and molecular line emission have shown the central-concentrated morphology of dust and gas density structure of the IRAS 18317-0513 region and an absence of a neighbor object around it (Faúndez et al. 2004; López-Sepulcre et al. 2010) as shown in Figure 2.5.

Its distance is 3.0 kpc obtained in the RMS project (Lumsden et al. 2013) although it has large uncertainty, typically $\pm$ 1 kpc, in the observations by this project because this is a kinematic distance of molecular gas (Urquhart et al. 2008a). The IRAS 18317-0513 region consists of two objects. The one is brighter in the NIR and also the MIR at the N-band wavelengths and the other, located at south-east of the brighter one, is NIR-fainter object (Lumsden et al. 2013) as shown in Figure 2.6. The separation between two objects is about 4.7 arcsec and it corresponds to $1.4 \times 10^4 AU$. The free-free emission in the centimeter wavelengths has not been reported in this region (Urquhart et al. 2009; Lumsden et al. 2013). Weak SiO outflow has been detected in this region and expected to be associated with the NIR-bright object but HCO+, which is considered as a strong accretion tracer, is not detected (López-Sepulcre et al. 2011). These observational results suggest that an accretion activity of this NIR-bright object is modest at present and this object may be at the later phase of massive star formation in the pre-main sequence stage (López-Sepulcre et al. 2011). However, it has not been confirmed whether SiO outflow actually comes from the NIR-bright object or not because these radio observations have been carried out with relatively low spatial resolution.

2.3 Standard stars

Careful evaluation of point spread functions is critical to obtain feasible images of crowded regions such as close objects and elongated structure. We have observed infrared bright stars selected from IRAS-PSC with the criteria of $F_{25\mu m} \geq 500 Jy$. (See Table 2.4; we call them PSF standards). The observations of the PSF standards have been carried out at nearly the same airmass of the targets.

Some of the PSF standards are also used for the calibration of the photometry. These stars are known as variable stars and their intrinsic fluxes are generally unclear. To reduce the uncertainty of the intrinsic fluxes, other stars known as the MIR photometric standards described in Cohen et al. (1999) have also been observed at the N-band. The uncertainty of photometry with PSF standards are described in detail in Chapter 3.

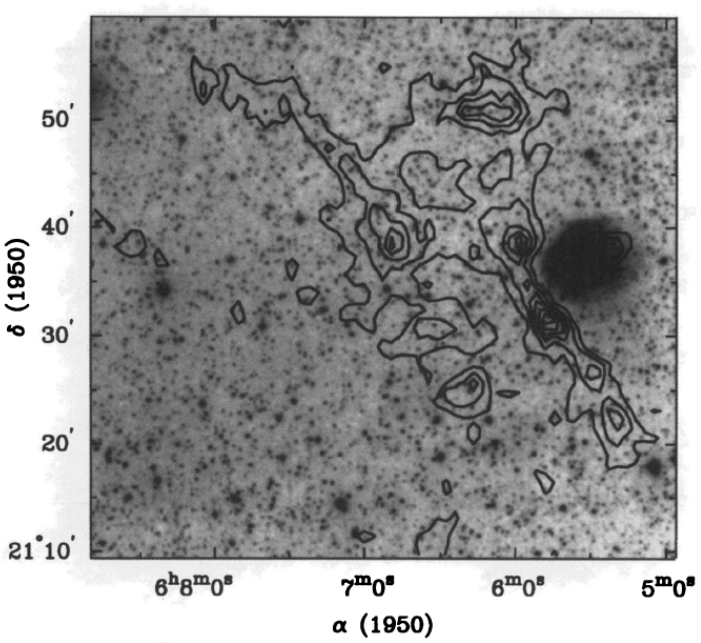

Figure 2.3: The image around the Sh 247 HII region from the observations of Carpenter et al. (1995). Gray scale map corresponds to a digitized red Palomar Sky Survey print. A bright object located at west side is Sh 247 HII region. Black contours represent peak antenna temperature of $^{13}CO(2-1)$ with increment of 1.0 K from 1.5 K corresponding to the observational noise temperature. The RAFGL 6366S region is located at about 10 arcmin south-east from the S247 HII region.

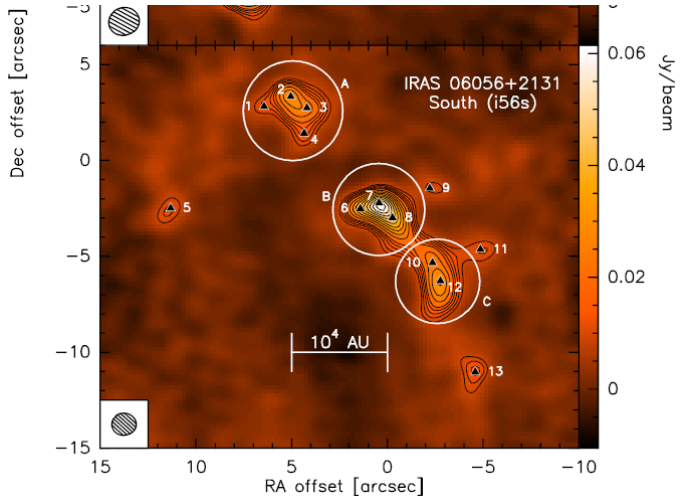

Figure 2.4: The image of the RAFGL 6366S region at 1.4 millimeter from the Rodon (2009). The contours start at the 4 σ level in both panels, increasing in 1 σ steps up to the 8 σ contour and in 2 σ steps afterwards. The UCHII region is detected at the region A. The MSX source corresponds to the region B. The region C is only detected at radio wavelengths and infrared-quiet region.

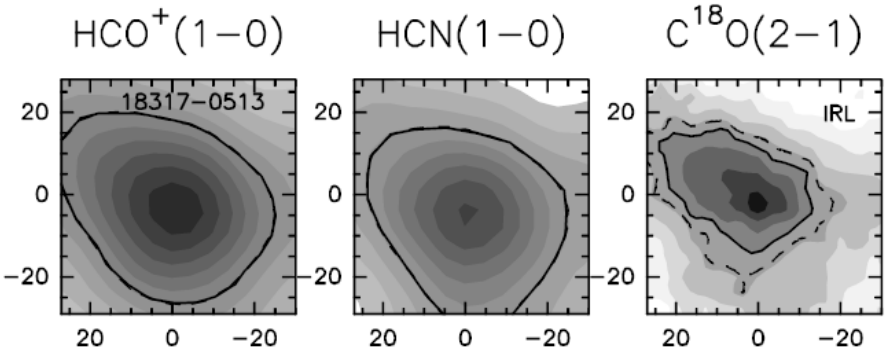

Figure 2.5: The images of the IRAS 18317-0513 region observed with $HCO^+(1-0)$, $HCO(1-0)$, and $C^{18}O(2-1)$ from the López-Sepulcre et al. (2010). The unit of the axises are arecsecs offset from the center of the peak of 1.2 mm observations. The central-concentrated morphology of gas density can be seen in all molecular line emissions.

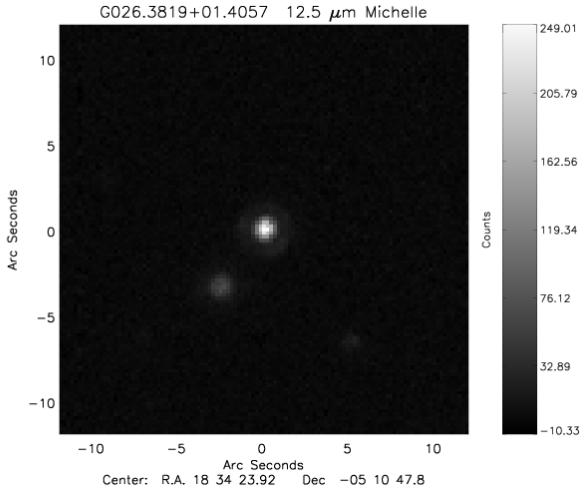

Figure 2.6: The images of the IRAS 18317-0513 region observed at 12.5 micron (Lumsden et al. 2013). Two objects, bright one and faint one, are clearly seen. The bright object is also brighter at the NIR wavelengths estimating from the 2MASS map.

Table 2.4: miniTAO/MAX38 Observation

Object	R.A.[1](J2000)	Dec[1](J2000)	Date	Filter	Int.time[sec]	PWV[mm][2]	Airmass	Chopping
IRC+10420[3]	$19^h\ 26^m\ 48.^s1$	$11^\circ\ 21'\ 16''$	2010/9/19	31μm	500	0.60	1.23	32”
				18μm	100	0.60	1.23	
			2011/5/27	25μm	100	0.50	1.43	38”
			2011/11/04	31μm	200	0.35	1.21	20”
				18μm	50	0.35	1.22	
				12μm	50	0.35	1.22	
V1185 Sco[4]	$17^h\ 44^m\ 24.^s0$	$-31^\circ\ 55'\ 35''$	2011/5/27	37μm	1000	0.45	1.03	38”
VY CMa[5]	$07^h\ 22^m\ 58.^s3$	$-25^\circ\ 46'\ 03''$	2011/10/31	31μm	100	0.85	1.00	20”
				18μm	100	0.85	1.00	
				12μm	10	0.85	1.00	
WX Psc[6]	$01^h\ 06^m\ 26.^s0$	$12^\circ\ 35'\ 53''$	2011/11/01	8.9μm	10	1.05	1.50	20”
α Ori[7]	$05^h\ 55^m\ 10.^s3$	$07^\circ\ 24'\ 25''$	2012/10/24	25μm	100	0.50	1.22	38”
				37μm	600	0.50	1.19	

[1] http://simbad.u-strasbg.fr/simbad/

[2] PWV values were obtained from APEX weather data archive (http://www.apex-telescope.org/weather/) and modified to the values of observing site using the method shown in Miyata et al. (2012)

[3] Mid-A type massive red supergiant.

[4] O-star and Mira.

[5] Massive red supergiant.

[6] Late-M type AGB star and O-star.

[7] M2 type O-rich supergiant.

2.4 Data reduction

In data reduction, a weighted-average method (Nakamura 2011) is used for reducing background noise. This method can subtract atmospheric emission by empirical estimation. It is confirmed that patterns on a image due to atmospheric turbulence can be eliminated in the works by Nakamura (2011). This method is quite useful and efficient especially for spatially extended sources and achieves a higher signal-to-noise ratio than a simply averaging method without any loss of the flux. After that, all the four images of chopping and nodding beams have been added into one image.

Chapter 3

Result

3.1 Mid-infrared morphology

3.1.1 M8E

Figure 3.1 shows images of the M8E region at 18, 25, 31, and 37 μm. The M8E region has been detected above 3 σ of the background sky noise in all observing bands as seen in Figure 3.1 (see dashed lines). Images of PSF reference stars, IRC+10420 and V1185 Sco, are also displayed in the figure. A bright object seems to be detected at the position of the M8E region. It is clearly resolved into two sources at 25 μm, while it is marginally resolved at 31 and 37 μm. The separation of the two peaks is approximately 7 arcsec. Halo-like structure with a radius of approximately 10 arcsec is seen in the images of the M8E region at 18 and 25 μm, but the similar structure is also seen in the images of the PSF reference star, indicating that it is not real structure of the object.

Previously mid-infrared images obtained at 10 and 24.5 μm with the Subaru/COMICS have been reported by de Wit et al. (2009) and Linz et al. (2009). These images have achieved high spatial resolution, less than 1 arcsec. They have resolved the M8E region and shown that this region consists of three point-source like objects, a compact and bright M8E-IR, a cometary-shaped M8E-radio (Simon et al. 1984), and a previously undetected source. The positions of the three objects are marked in Figure 3.1 (b) assuming that the flux peak position in Figure 3.1 (b) corresponds to the position of the brightest object in the M8E region at 24.5 μm, M8E-IR, in the previous work of de Wit et al. (2009). This comparison gives a good agreement with our 25 μm image obtained with the miniTAO/MAX38. The result suggests that two peaks resolved in our 25 μm image correspond to M8E-IR and M8E-radio in the image of de Wit et al. (2009), respectively. No sources corresponding to the third object (shown as a triangle mark) are found in our images. This non-detection of the third object is consistent with the fact that the third object is much fainter than M8E-IR and M8E-radio in the previous observations (Linz et al. 2009; de Wit et al. 2009). Our and previous results have suggested that the third component accounts for little in the total luminosity of the whole M8E region. Therefore, the third object will not be studied and analyzed in detail in this work later.

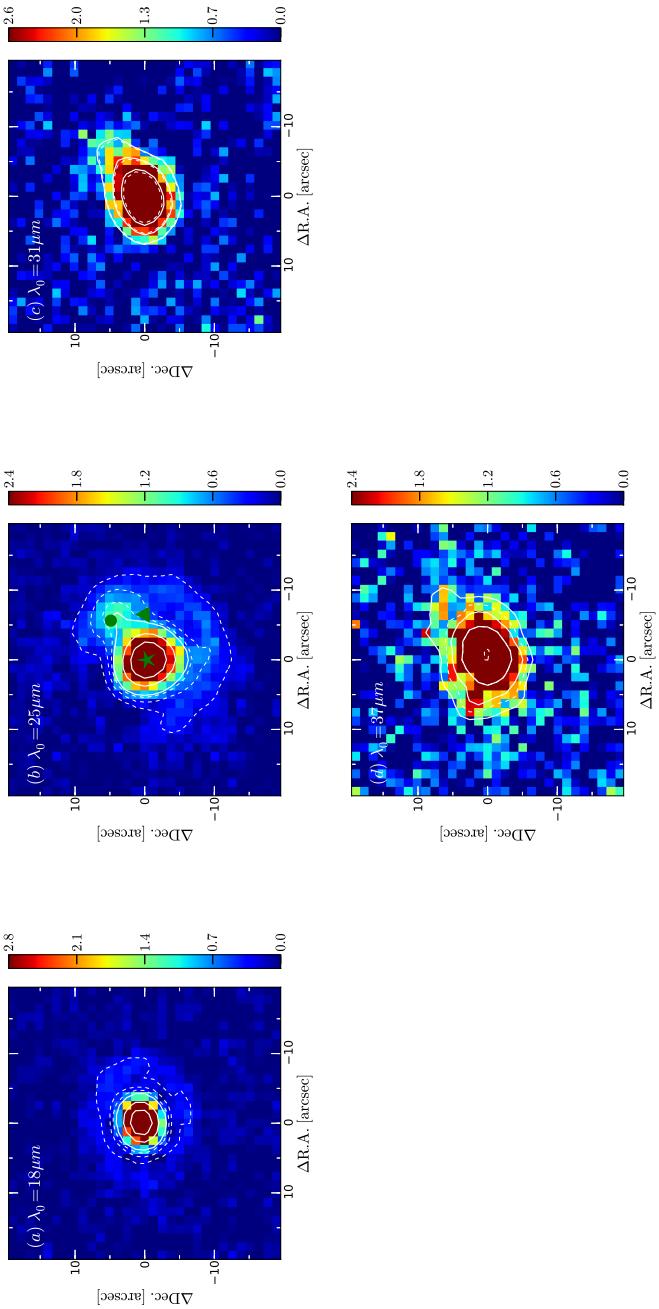
(a) λ0=18μm
(b) λ0=25μm
(c) λ0=31μm
(d) λ0=37μm
ΔDec. [arcsec]
ΔR.A. [arcsec]
10
0
−10
2.8
2.1
1.4
0.7
0.0
2.6
2.0
1.3
0.7
0.0
2.4
1.8
1.2
0.6
0.0

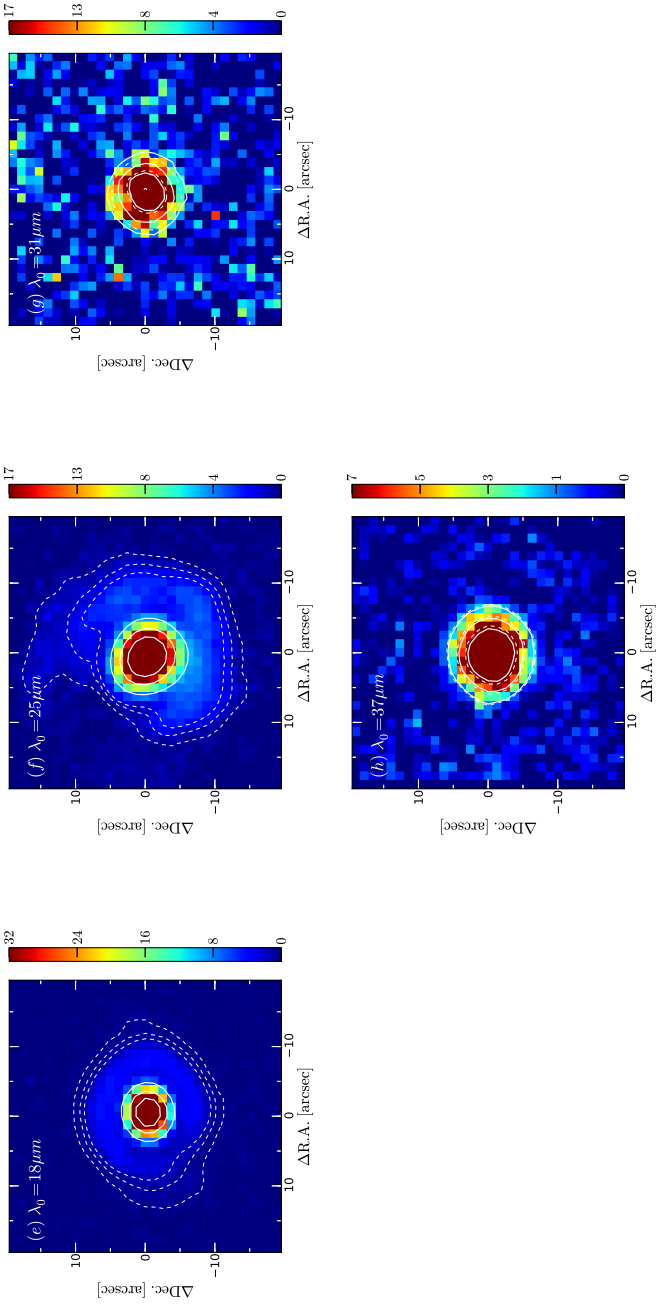

Figure 3.1: Mid-infrared images of M8E (Top) and PSF standard (Bottom) observed with the MAX38. Field of view is 40" × 40" in all images and North is up. The center position of each image corresponds with the flux peak position of each image. The unit represents in color-scale is [Jy/$arcsec^2$]. The (a), (b), (c), and (d) images of M8E correspond with images of 18, 25, 31, and 37 μm respectively. Also, the (e), (f), (g), and (h) images of PSF standards correspond with images of 18, 25, 31, and 37 μm respectively. PSF standards are IRC+10420 in (e), (f), and (g) and V1185 Sco in (h). Dash lines represent 3σ, 6σ, and 9σ contour of background noise. Solid lines represent 20% , 40% , and 60% contour of peak counts. In all wavelengths, extended north-west structure can be seen in M8E region as compared with PSF standards. In the (b) image, ⋆ mark, • mark, and △ mark show the positions of M8E-IR, M8E-radio, and the third brightest source of M8E region in 24.5 μm described in de Wit et al. (2009)

3.1.2 RAFGL 6366S

Figure 3.2 shows images of the RAFGL 6366S region at 8.9, 12, 18, 25, 31, and 37 μm, together with those of the PSF reference stars, WX Psc, VY CMa, and α Ori. As compared with dashed lines in Figure 3.2, it is confirmed that the RAFGL 6366S region has been detected above 3 σ of the background sky noise in all observing bands.

Two objects can be clearly seen at 18 and 25 μm, while they are marginally resolved at 31 and 37 μm. The separation of the two peaks is approximately 8 aecsec. In the 12 μm image, the source is clearly elongated but its direction from north-west to south-east is not consistent with the direction of the two objects seen in the 18 and the 25 μm images. At 8.9 μm, the detected source seems to be a single point source. The images of the PSF references at 31 and 37 μm (Figure 3.2 (k) and (l)) are slightly elongated. This may be caused by imperfect focusing of the telescope. However, the elongation of the PSF images is much smaller than the extension of the target images and we consider that the extension of the target is not artificial but real structure.

Hereafter, the central bright object seen in the all wavelengths and the second object only seen at 18, 25, 31, and 37 (marginally) μm are called as RAFGL 6366S-IR1 and RAFGL 6366S-IR2, respectively. Previous observations in the millimeter-radio and the NIR wavelengths with high spatial resolution, less than 5 arcsec, have revealed that this region should consist of three objects in the MIR, the object with the UCHII region, the MYSO, and the NIR object considered as a low mass YSO (Rodon 2009). Their positions are marked in Figure 3.2 (c) assuming that the flux peak position in Figure 3.2 (c) corresponds to the position of the brightest object in the RAFGL 6366S region in the MIR and the millimeter wavelengths, the previously detected MYSO in the work of Rodon (2009). The positions of the object with the UCHII region and the MYSO in the previous observations almost correspond to those of IR2 and IR1 in our 18 μm image, while our observations cannot resolve the MYSO and the NIR object in 18 μm and longer wavelengths due to insufficient spatial resolution. This result suggests that IR1 corresponds to the complex of the MYSO and the NIR object and IR2 corresponds to the object with the UCHII region. IR1 is partly spatially resolved into two sources of the MYSO and the NIR object at 12 μm. IR2 cannot be seen at 8.9 and 12 μm, which may be due to the strong extinction of silicate in this region.

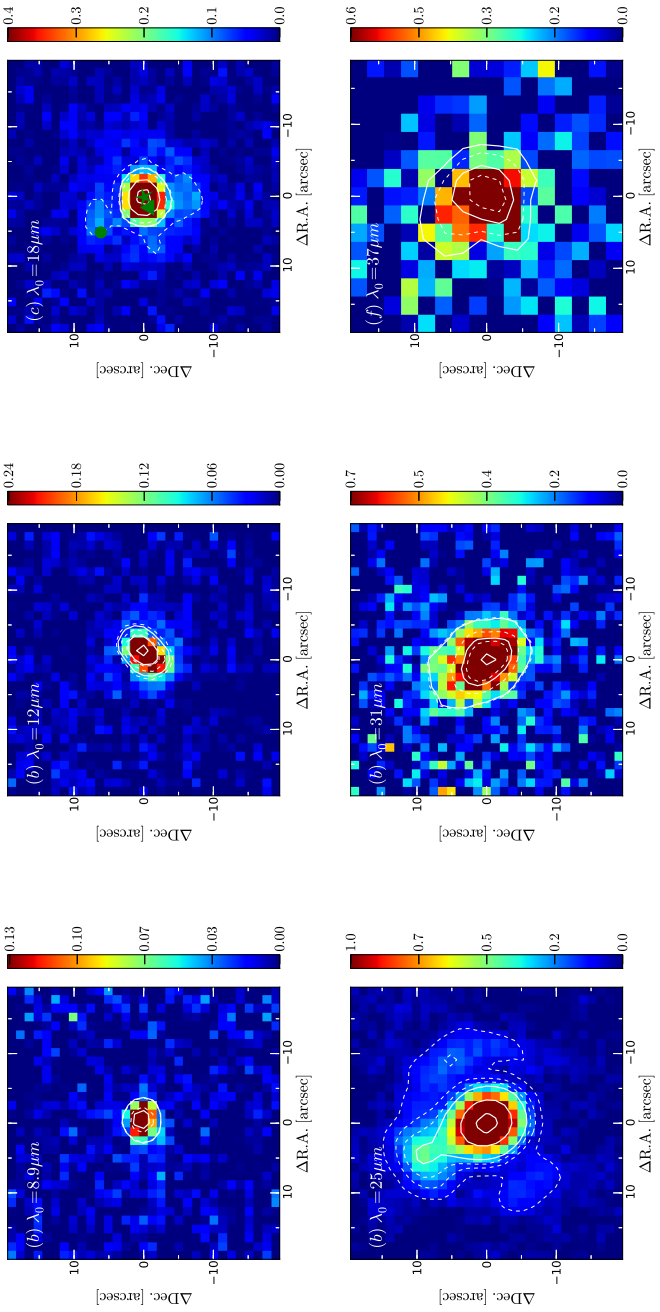
(c) $\lambda_0 = 18\mu m$
(f) $\lambda_0 = 37\mu m$
(b) $\lambda_0 = 12\mu m$
(b) $\lambda_0 = 31\mu m$
(b) $\lambda_0 = 8.9\mu m$
(b) $\lambda_0 = 25\mu m$
ΔR.A. [arcsec]
ΔDec. [arcsec]

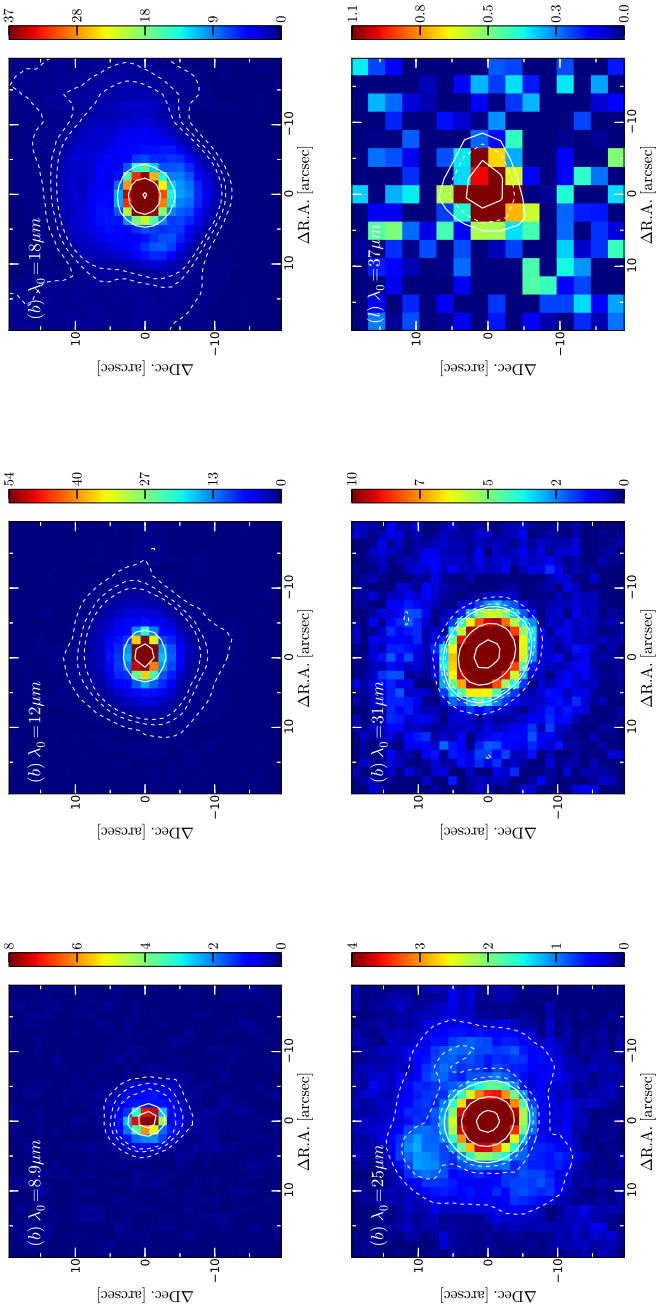

Figure 3.2: Mid-infrared images of RAFGL6366S (Top) and PSF standard (Bottom) observed with the MAX38. Field of view is 40" × 40" in all images and North is up. The center position of each image corresponds with the flux peak position of each image. The unit represents in color-scale is [Jy/$arcsec^2$]. The (a), (b), (c), (d), (e), and (f) images of RAFGL 6366S correspond with images of 8.9, 12, 18, 25, 31, and 37 μm respectively. Also, the (g), (h), (i), (j), (k), and (l) images of PSF standards correspond with images of 8.9, 12, 18, 25, 31, and 37 μm respectively. In addition, both RAFGL 6366S and PSF standards do not have high signal to noise ratio in 37 μm images. Therefore, 2 pix*2 pix binning has been performed to both images. PSF standards are WX Psc in (g), VY CMa in (h), (i), and (k), and α Ori in (j) and (l). Dash lines represent 3σ, 6σ, and 9σ contour of background noise. Solid lines represent 20% , 40% , and 60% contour of peak counts. In (c) and (d) images, extended north-east structure can be seen in RAFGL 6366S region. In (c) image, $\star$ mark, $\bullet$ mark, and $\triangle$ mark represent the positions of MYSO (RAFGL 6366S-IR1), UCHII (RAFGL 6366S-IR2), and near-infrared object detected in Rodon (2009), respectively.

3.1.3 IRAS 18317-0513

Figure 3.3 shows images of the IRAS 18317-0513 region and the PSF reference star, IRC+10420, at 12, 18, and 31 μm. It is shown that the IRAS 18317-0513 region has been detected above 3 σ of the background sky noise in all observing bands in comparison with dashed lines in Figure 3.3. Two objects are marginally resolved in all wavelengths.

The two infrared objects have been detected in observations with high spatial resolution, less than 2 arcsec, in Urquhart et al. (2009). Their positions are marked in Figure 3.3 (b) assuming that the flux peak position in Figure 3.3 (b) corresponds to the position of the brightest object in the IRAS 18317-0513 region in the NIR in the previous work of Urquhart et al. (2009). Our $18\mu m$ image is well consistent with the previous results when comparing the positions of the two objects. Hereafter, the objects at the north-west side and at the south-east side are called as IRAS 18317-0513-IR1 and IRAS 18317-0513-IR2, respectively.

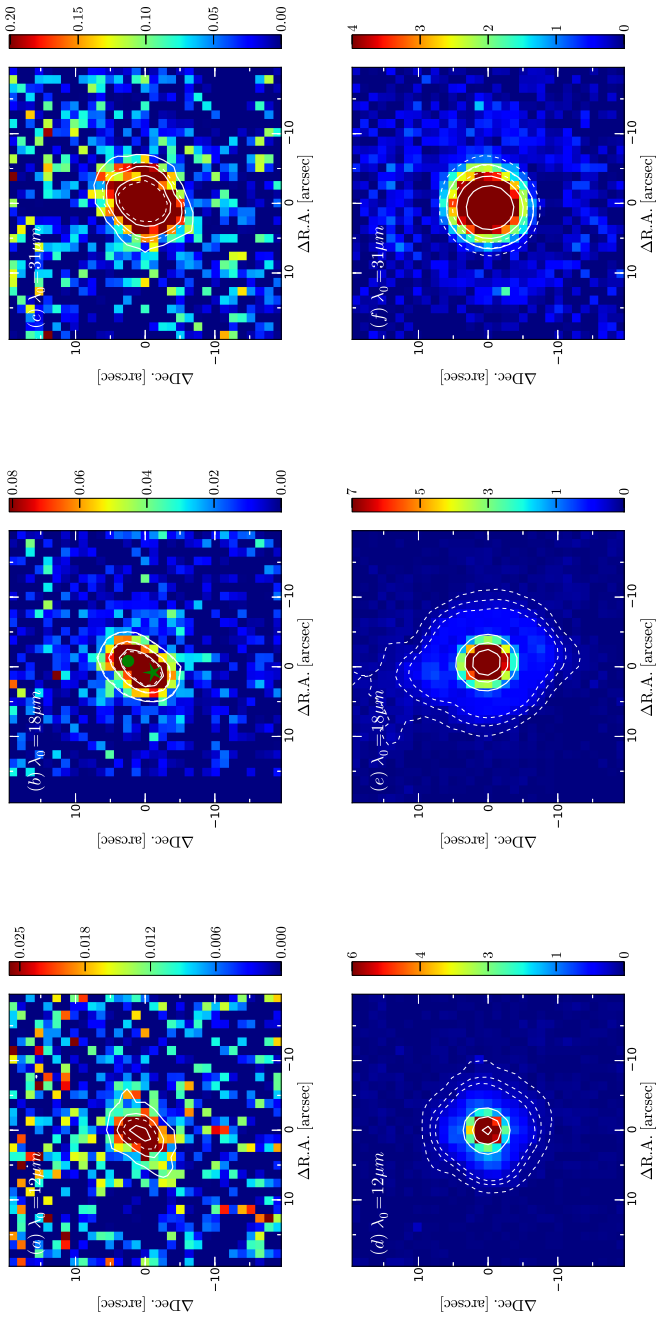

Figure 3.3: Mid-infrared images of IRAS 18317-0513 (Top) and PSF standard (Bottom) observed with the MAX38. Field of view is 40" × 40" in all images and North is up. The center position of each image corresponds with the flux peak position of each image. The unit represents in color-scale is [Jy/$arcsec^2$]. The (a), (b), and (c) images of IRAS 18317-0513 correspond with images of 12, 18, and 31 μm respectively. Also, the (d), (e), and (f) images of PSF standards correspond with images of 12, 18, and 31 μm respectively. PSF standards are IRC+10420 in all wavelengths. Dash lines represent 3σ, 6σ, and 9σ contour of background noise. Solid lines represent 20% , 40% , and 60% contour of peak counts. In all wavelengths, extended north-west structure can be clearly seen in IRAS 18317-0513 as compared with PSF standards. In (b) image, $\star$ mark represents the near-infrared brightest object (IRAS 18317-0513-IR1) in previous work Urquhart et al. (2009) and $\bullet$ mark represents the second one (IRAS 18317-0513-IR2) in this region.

3.2 PSF Photometry

3.2.1 Flux measurements

In each observed region, two objects have been detected with our observations. To obtain the flux of the individual object accurately, PSF photometry has been performed. The model PSFs have been made by the images of the PSF standard stars. When the second brightest object is not clearly resolved and the position of the object is difficult to be determined, the relative position measured in other wavelengths is used. We note that the flux measured here is a just relative one, and further calibration is needed for the absolute photometry (see the next subsection). The measured flux ratios of the two objects are listed in Table 3.1.

To evaluate the validity of the PSF photometry, model-reproduced images have been made by the combination of the two best-fitted model PSFs and subtracted from the observed images at each observing band in each region. The standard deviation of the subtracted images in object-subtracted area is almost consistent with that in the background sky area as seen in Table 3.1. In addition, there seems to be no artificial structure in the subtracted images. These suggest that the observed images consist of two point-source objects and another objects or the extended structure are not included in the images. One exception is the image of the RAFGL 6366S region at 12 μm. It shows significantly large standard deviation. This may be caused by the fact that RAFGL 6266S-IR1 is not a single point source but it consists of two objects, the MYSO and the NIR object, as already mentioned in the previous section.

Table 3.1: The result of the separation performances.

Object	Filter	flux ratio[1]	Standard deviation of object-subtracted area [mJy/$arcsec^2$]	Background sky standard deviation [mJy/$arcsec^2$]
M8E	18μm	0.028 $\pm$0.006	63	60
	25μm	0.14 $\pm$0.01	94	57
	31μm	0.24 $\pm$0.03	320	330
	37μm	0.23 $\pm$0.02	310	360
RAFGL 6366S	8.9μm	0.03 $\pm$0.03	40	37
	12μm	0.03 $\pm$0.08	76	49
	18μm	0.07 $\pm$0.03	69	60
	25μm	0.1 $\pm$0.1	40	34
	31μm	0.21 $\pm$0.03	330	330
	37μm	0.31 $\pm$0.06	690	690
IRAS 18317-0513	12μm	0.36 $\pm$0.02	19	18
	18μm	1.2 $\pm$0.1	35	33
	31μm	1.3 $\pm$0.1	140	140

[1] The flux ratio of the faint object to the bright object. The bright object means M8E-IR, RAFGL 6366S-IR1, and IRAS 18317-0513-IR1 in each region.

3.2.2 Absolute flux calibration

Absolute fluxes of the objects have been calibrated with the observations of the PSF standard stars just before or after the target observations. Measurements by the ISO/SWS have been employed as the intrinsic fluxes of these stars. However, these stars are long period variables and their intrinsic fluxes at the observing time are expected to be different from the ISO measurements. In this study, these stars have also been observed in the N-band and calibrated with the measurements of the non-variable stars listed as the MIR standard stars in Cohen et al. (1999). For data of α Ori, observations in the N-band have not been conducted with the miniTAO/MAX38 and the calibration using the MIR standard stars has not been available. On the other hand, Jupiter has been observed at 31 μm in the same day. Flux of Jupiter has been obtained by interpolation of DIRBE data (Hauser et al. 1991) and calibrated by an apparent diameter in the observed day assumed that the brightness temperature of Jupiter is stable. This assumption seems to be feasible because the brightness temperature of Jupiter does not vary larger than 0.6 % in seven-year monitoring in the millimeter wavelengths (Weiland et al. 2011). In addition, although the stability of the brightness temperature of the Jupiter in the MIR is not understood well, the flux of Jupiter in the MIR obtained with DIRBE is stable, within the error of 2 %, during two months monitoring when calibrated by an apparent diameter in the observed day (Kamizuka in private communication). Therefore, we adopt Jupiter as a calibrator of α Ori in this work. The error of DIRBE flux is about 2 % as mentioned above and we assume the same flux error of Jupiter in our calculation.

In addition, we have assumed that the colors of the PSF Standard stars have not changed during the flux variations of the stars. Monnier et al. (1998) have monitored the color variations of long period variables including our PSF standard stars, IRC+10420, WX Psc, α Ori, and VY CMa in 3 years from 8 to 13 μm and revealed that the color variation was almost negligible in these wavelengths. Although the color variation of the Mira-type star V1185 Sco is observationally unknown, Smith (2003) has shown that Mira-type variables generally show small color variation, approximately 10 %. Total uncertainness of the intrinsic flux estimation is considered to be less than 10 %. The derived fluxes of the PSF standards from these calibrations are listed in Table 3.2.

The other issue to be considered is systematic errors from unstable atmospheric conditions in the MIR wavelengths during the observations of the targets and the standards. To estimate variation of atmospheric transmittance, the ATRAN (Lord 1992) model has been used. Even if the PWV drastically varies from 0.5 mm to 1.0 mm during the observations, the variation of the transmittance at 18 and 25 μm is less than 10 % and 30 %, respectively. Since the observations have been carried out under more stable conditions as listed in Tables 2.3 and 2.4, these variations (< 10 % at 18 μm and < 30 % at 25 μm) are considered to be upper limits.

In the longer wavelength range, 31 and 37 μm, the variation should be much larger because the atmospheric transmittance relatively largely depends on the PWV in these wavelengths (Asano 2011). The variation of the atmospheric transmittance causes the variation of the background fluxes directly because this wavelength range is on the Rayleigh-Jeans side of atmospheric thermal emission. The measured background fluxes varied typically within 5 % and 7 % in the worst case. Assuming that emission from the telescope is about 30 % of the whole background flux and that from the sky is about 70 % in the long-MIR wavelengths (Asano 2011), this background variation indicates that the variation of the relative atmospheric transmittance is typically less than 30 % (PWV less than 1.0 mm) and roughly 80 % on 30 October 2011 and 23 October 2012 under a bad weather condition (PWV equal to or more than 1.0 mm). This is briefly because 5 % variation of the background sky flux corresponds to 7 % change of absolute emissivity of the atmosphere and considering that typical atmospheric transmittance at 31 and

37 μm is about 30 % (Miyata et al. 2012), typical variation of the relative atmospheric transmittance is calculated as less than 30 %. The variations of the relative atmospheric transmittances in all observing dates have been calculated in the same way as shown above but the transmittance derived from the PWV of each day is used instead of the typical PWV value. Therefore, more realistic results of instability have been estimated and described above.

Derived flux of each object is listed in Table 3.3. The flux errors in Table 3.3 are only care about photometric errors from statistical origins.

For the M8E region, spectral data obtained by the ISO/SWS is also available. The beam size of ISO/SWS is 14" × 27" and M8E-IR and M8E-radio have not been resolved in this data. The flux derived from this is also listed in Table 3.3. In comparison with the flux of the M8E region derived from our observing data (Table 3.3), the difference is 1.2 %, 4.4 %, 20 % and 25 % in 18, 15, 31 and 37 μm, respectively. These differences seem to be explained by the uncertainty from the variation of the atmospheric transmittance as discussed above. Therefore, the fluxes and their errors derived in this work are reasonable. In the M8E region, the ISO/SWS flux are used for following analysis.

Table 3.2: Flux of PSF standards

PSF standard	wavelength(λ_o) [μm]	Flux [Jy]	calibrator
WX Psc	8.9	850	π^2 Aqr
VY CMa	12.2	9600	β Col
	18.7	12000	
	31.7	5100	
α Ori	24.5	790	
	31.7	550	Jupiter
	37.3	370	
IRC+10420	12.2	1100	
	18.7	2300	α Boo
	24.5	2400	
	31.7	1900	
V1185 Sco	18.7	630	α Boo
	37.3	1100	

Table 3.3: Fluxes of the objects from photometry result given in Jy.

Object	8.9μm	12.2μm	18.7μm	24.5μm	31.7μm	37.3μm
M8E-IR	-	-	183±2	306±3	436±10	341±6
	-	-	185±2[1]	293±3[1]	364±8[1]	455±8[1]
M8E-radio	-	-	5±2	43±3	107±10	79±6
	-	-	5±2[1]	41±3[1]	89±8[1]	105±8[1]
RAFGL 6366S-IR1	19.1±0.6	52±4	112±4	164±17	274±7	260±16
RAFGL 6366S-IR2	< 0.4	< 1.7	8±4	22±17	57±7	81±16
IRAS 18317-0513-IR1	-	6.4±0.4	15.9±0.7	-	53±3	-
IRAS 18317-0513-IR2	-	2.3±0.4	18.6±0.7	-	69±3	-

The flux errors only include statistical origins and not systematic ones.
[1] Flux derived from ISO/SWS spectral data of the M8E region.

3.3 Estimation of Luminosities

The luminosities of the observed objects are derived from SED including our photometric data. When deriving the luminosities of the MYSOs and the objects with the UCHII regions, it is assumed that all their radiation is absorbed and re-emitted by the warm dust in their surrounding circumstellar envelopes as mentioned in Chapter 1.

3.3.1 M8E

Spectral energy distributions of M8E-IR and M8E-radio are plotted in Figure 3.4. While M8E-IR has a relatively flat SED in the mid-infrared region, M8E-radio shows a curved SED and its peak is located at approximate 30 μm. In the MIR wavelengths, M8E-IR accounts for the most of the whole flux among the M8E region.

The SED of M8E-radio has been fitted by single-temperature blackbody radiation. Most of the fluxes have been well reproduced by the blackbody radiation with a temperature of 92 K (the solid line in Figure 3.4) except for the flux at 18 μm. The error of the temperature estimation is $\pm 4K$. The modeled flux at 18 μm is about 2 times higher than the observation. One possible explanation is foreground extinction. The visual extinction (A_v) of at least 30 mag is required to modify the modeled flux at 18 μm which is consistent with the observed one within the error, but it also decreases the flux at 25 μm down to about 30 % from the original one. The fitting cannot be improved even if both the temperature and the extinction are modified. Another possible explanation is internal structure of M8E-radio. M8E-radio is the deeply embedded object and it may not be able to be seen through internal region even at 18 μm. Since the outer region is expected to be cooler than the inner region, the flux at 18 μm would be observed to be fainter than expectation.

The derived bolometric luminosity of M8E-radio is $8 \times 10^2 L_\odot$ in total at the assumed distance of 1.5 kpc. The error of the derived luminosity due to the error of the derived temperature is estimated as $\pm 15\%$. In the wavelengths longer than 25 μm, the luminosity is estimated via integrating the blackbody of 92 K, while it is calculated by numerical integration of the observed fluxes from 18 to 25 μm. The contribution at the wavelengths shorter than 18 μm is neglected because it seems to be very small compared with the total luminosity.

It is clear that the fluxes in the wavelengths from the far-infrared to the sub-mm wavelengths show significant contribution to the total flux. It is usually observed that relatively cold components are associated with MYSOs and objects with UCHII regions and considered as extended diffuse components (Churchwell 2002). Unfortunately, no spatially resolved images have been taken yet from the far-infrared to the sub-mm in the M8E region. It is not clear which of M8E-IR or M8E-radio is the major source of the far-infrared/sub-mm emission. Adopting the temperature of 30 K, which is a typical temperature of the cold components associated with the MYSOs and the objects with the UCHII regions (Churchwell 2002), its total luminosity is estimated as $1 \times 10^3 L_\odot$ (see the chained line in Figure 3.4 in the case of all the cold component associated with M8E-radio). Assuming that the uncertainty of the temperature of the cold component is roughly $\pm 5K$, the uncertainty of its total luminosity is $\pm 50\%$. If all cold component associates with M8E-radio, this is an upper limit case of the contribution to the luminosity of the M8E-radio. Therefore, the total luminosity of M8E-radio is derived as $1.5 \pm 0.5 \times 10^3 L_\odot$.

Previously, de Wit et al. (2009) have estimated the total luminosity of this region as $8 \times 10^3 L_\odot$. This has been based on the unresolved photometric data in the wavelengths longer than 25 μm, and it includes the luminosities of both M8E-IR and M8E-radio. Therefore, the luminosity of M8E-IR is estimated as $6.5 \pm 0.5 \times 10^3 L_\odot$.

The uncertainty of the distance towards the M8E region also affects the absolute luminosity

of the two object, while a ratio of the luminosities between the two objects does not change. When the distance is 1.25 kpc, the closest case, the luminosities of M8E-radio and M8E-IR are estimated as $9 \pm 4 \times 10^2 L_\odot$ and $4.5 \pm 0.4 \times 10^3 L_\odot$, respectively.

3.3.2 RAFGL 6366S

SEDs of RAFGL 6366S-IR1 and RAFGL 6366S-IR2 are shown in Figure 3.5. While IR1 has a relatively flat SED in the mid-infrared region, IR2 shows a curved SED and its peak is about $30\mu m$. IR1 accounts for the most of the whole flux of the RAFGL 6366S region in the mid-infrared wavelengths.

At wavelengths longer than 18 μm, the SED of IR2 has been well reproduced by the single-temperature blackbody radiation with a temperature of $87 \pm 3K$ (the solid line in Figure 3.5).

The derived bolometric luminosity of IR2 is $1.1 \times 10^3 L_\odot$ in total at the assumed distance of 2.0 kpc. In the wavelengths longer than 37 μm, the luminosity is estimated via integrating the blackbody of 87 K, while it is calculated by numerical integration of the observed fluxes from J band to 37 μm. In this calculation, we ignore the fluxes upper limits at 8.9 and 12 μm and using the linear interpolation between the fluxes at K band and 18 μm because the fluxes at 8.9 and 12 μm may suffer severe silicate extinction. The contribution at the wavelengths shorter than J band is neglected because it seems to be very small compared with the total luminosity. The error of the derived luminosity is estimated as $\pm 17\%$.

For IR1, the SED has been well reproduced by the single-temperature blackbody radiation with a temperature of $145 \pm 9K$ (the dashed line in Figure 3.5).

The derived bolometric luminosity of IR1 is $4.6 \times 10^3 L_\odot$ in total. The luminosity of IR1 has been calculated as the same way of IR2 but including the fluxes at 8.9 and 12 μm in the numerical integration. The error of the derived luminosity is estimated as $\pm 24\%$.

The fluxes at the far-infrared wavelengths from 58 to 150 μm show significant excess. Since these were measured with large beam sizes of > 1 arcmin, they may come from the diffuse region around the RAFGL 6366S core. The excessed sub-mm fluxes were also measured with relatively small apertures of 31 and 15 arcsec in Dunham et al. (2010) and Klein et al. (2005), respectively. This indicates that the fluxes come from the central core of RAFGL 6366S, but it is unclear which of IR1 or IR2 is the emitting source. Assuming the temperature of 30 K, it corresponds to the luminosity of $2.0 \times 10^2 L_\odot$. The uncertainty of its luminosity is assumed as $\pm 50\%$ in the same way of the M8E region. This is also considered as uncertainness of the total flux of IR1 and IR2, i.e., $4.8 \pm 1.3 \times 10^3 L_\odot$ and $1.3 \pm 0.4 \times 10^3 L_\odot$, respectively.

The uncertainty of the distance towards RAFGL 6366S region also affects the absolute luminosities of IR1 and IR2. When the distance is 1.0 kpc, the closest case, the luminosities of IR1 and IR2 are $1.2 \pm 0.3 \times 10^3 L_\odot$ and $3.3 \pm 1.0 \times 10^2 L_\odot$, respectively. When the distance is 3.0 kpc, the furthest case, those of IR1 and IR2 are $1.1 \pm 0.3 \times 10^4 L_\odot$ and $3.0 \pm 0.9 \times 10^3 L_\odot$, respectively.

3.3.3 IRAS 18317-0513

SEDs of IRAS 18317-0513-IR1 and IRAS 18317-0513-IR2 are plotted in Figure 3.6. While IR1 shows a strong excess in the near infrared region, IR1 and IR2 have roughly the same fluxes in the mid-infrared region.

At wavelengths longer than 12 μm, the SED of IR2 has been well reproduced by the single-temperature blackbody radiation with a temperature of $119 \pm 4K$ (the dashed line in Figure 3.6).

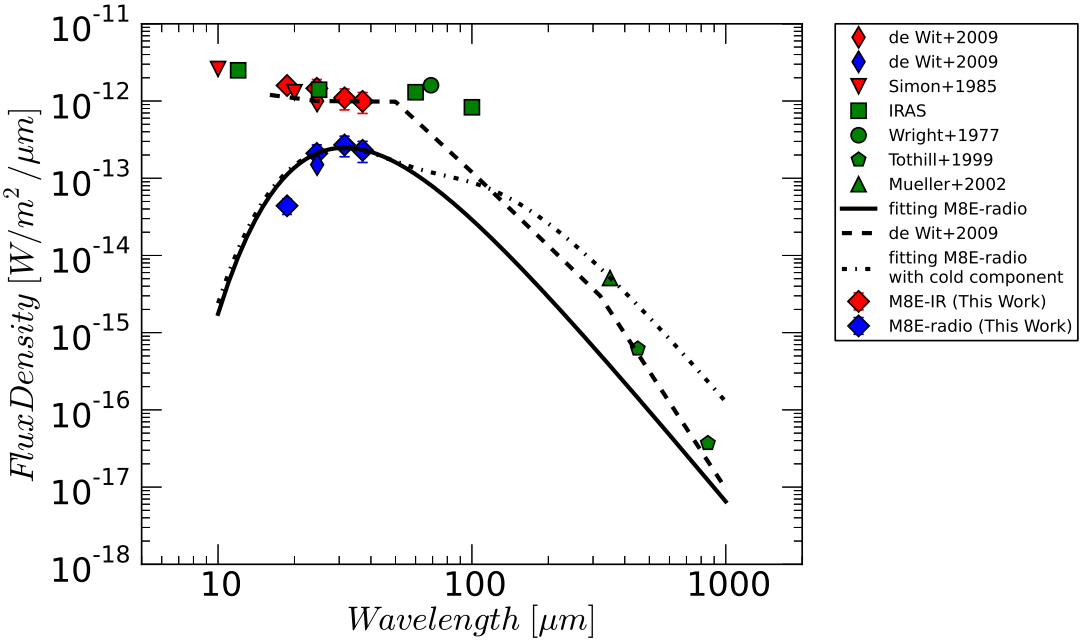

Figure 3.4: SED of M8E. Red, blue, and green mark represent M8E-IR, M8E-radio and unresolved flux, respectively. The data from this work is plotted as ⋄ mark. Solid line shows black body SED fitting of M8E-radio. Dashed line shows SED fitting of M8E-IR by de Wit et al. (2009). Chain line shows upper limit of the subtraction of M8E-radio submm flux from total submm flux. This limitation was fitted by 30 K black body radiation.

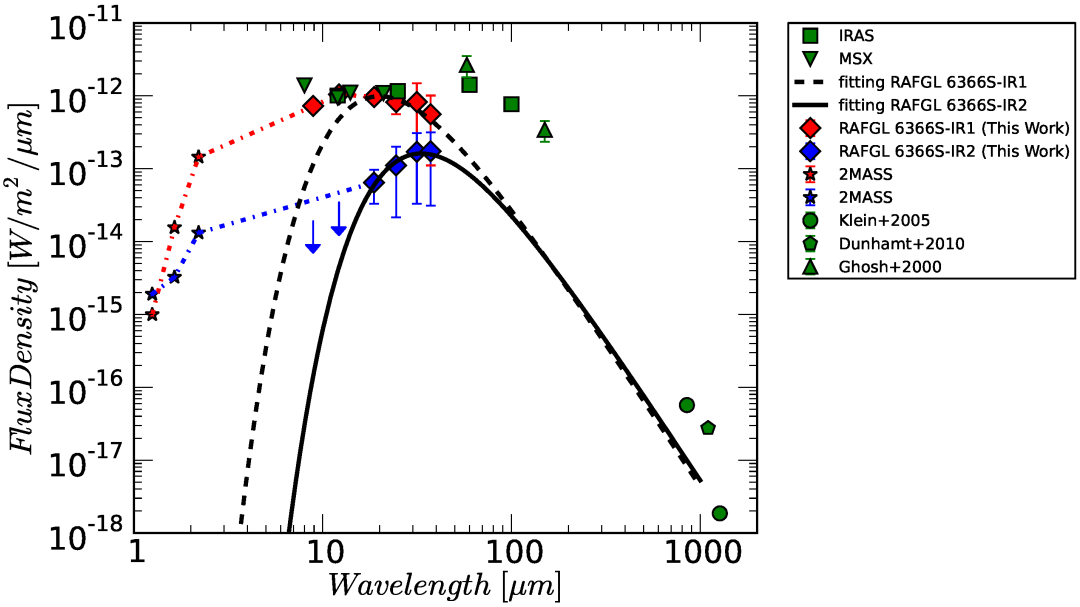

Figure 3.5: Result of SED fitting to RAFGL 6366S IR1 and IR2. Red, blue, and green mark represent fluxes of RAFGL 6366S-IR1, RAFGL 6366S-IR2, and unresolved total RAFGL 6366S region, respectively. The fluxes obtained by our work is plotted as $\diamond$ mark. Solid line represents black body radiation fitting of IR2 and dotted line represents that of IR1. The red chain line shows linear fitting of IR1's flux in shorter wavelengths and the blue one shows IR2's.

The derived bolometric luminosity of IR2 is $2.4 \times 10^3 L_\odot$ with an error of $\pm 7\%$ in total at the assumed distance of 3.0 kpc. In the wavelengths longer than 31 μm, the luminosity is estimated via integrating the blackbody of 119 K, while it is calculated by numerical integration of the observed fluxes from 12 to 31 μm. The contribution at the wavelengths shorter than 12 μm is neglected because it seems to be very small compared with the total luminosity.

For IR1, in the wavelengths longer than 31 μm, the luminosity has been tried to be estimated via fitting and integrating the blackbody radiation in the same way as IR2. However, the obtained fluxes are relatively flat from 12 to 31 μm and the SED fitting by single-temperature blackbody radiation cannot reproduce the observed fluxes well. Therefore, we have assumed $119 \pm 4K$ blackbody radiation from IR1, the same as IR2, and fitted the intensity of the radiation using the fluxes at 18 and 31 μm because the fluxes of IR1 at the 18 and 31 μm are almost the same values as those of IR2.

The derived bolometric luminosity of IR1 is $2.7 \times 10^3 L_\odot$ with an error of $\pm 9\%$ in total. The luminosity of IR1 has been calculated as the same way of IR2 but using the fluxes from J band to 31 μm in the numerical integration.

The fluxes at the far-infrared wavelength from 60 and 100 μm show significant excess, but these were measured with large beam sizes of > 1 arcmin and they may not come from the central core. The excessed sub-mm flux was also measured with a relatively small aperture of 24 arcsec (Faúndez et al. 2004). It would come from the IRAS 18317-0513 core, but it is unclear which of IR1 or IR2 is the emitting source. Assuming the temperature of 30 K, it corresponds to the luminosity of $5.9 \times 10^2 L_\odot$ with an error of $\pm 50\%$. This is also considered as uncertainness of the total flux of IR1 and IR2, i.e., $3.2 \pm 0.7 \times 10^3 L_\odot$ and $2.9 \pm 0.7 \times 10^3 L_\odot$, respectively.

The uncertainty of the distance towards IRAS 18317-0513 region also affects the absolute luminosities of IR1 and IR2. When the distance is 2.0 kpc, the closest case, the luminosities of IR1 and IR2 are $1.3 \pm 0.3 \times 10^3 L_\odot$ and $1.2 \pm 0.3 \times 10^3 L_\odot$, respectively. When the distance is 4.0 kpc, the furthest case, those of IR1 and IR2 are $5.8 \pm 1.3 \times 10^3 L_\odot$ and $5.2 \pm 1.3 \times 10^3 L_\odot$, respectively.

The summary of the luminosity estimation is listed in Table 3.4.

Table 3.4: Luminosities derived from SED.

Object	Evolutional stage	Luminosity ($L_\odot$)
M8E-IR	MYSO	$6.5 \pm 0.5 \times 10^3$
M8E-radio	UCHII	$1.5 \pm 0.5 \times 10^3$
RAFGL 6366S-IR1	MYSO	$4.8 \pm 1.3 \times 10^3$
RAFGL 6366S-IR2	UCHII	$1.3 \pm 0.4 \times 10^3$
IRAS 18317-0513-IR1	MYSO	$3.2 \pm 0.7 \times 10^3$
IRAS 18317-0513-IR2	MYSO	$2.9 \pm 0.7 \times 10^3$

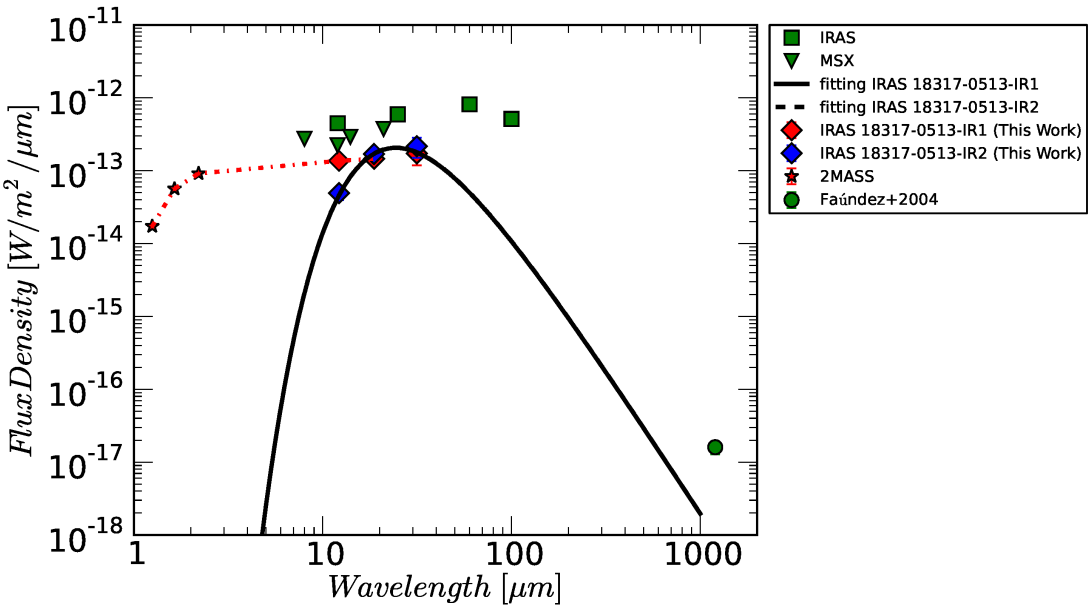

Figure 3.6: Result of SED fitting to IRAS 18317-0513 IR1 and IR2. Red, blue, and green mark represent the flux of IR1, IR2, and unresolved whole region, respectively. Fluxes obtained by this work is plotted as $\diamond$ mark. Solid line shows black body radiation fitting of IR1 and dotted line shows that of IR2. The red chain line represents linear fitting of IR1 in shorter wavelengths.

Chapter 4

Star formation sequences between HIYSOs and MYSOs

In this chapter, we will evaluate the masses of the individual objects and discuss their formation sequence in detail. The other star forming regions observed at a wide wavelength range with sufficient spatial resolution will also be searched in literatures to extend the number of samples.

4.1 Mass evaluation of individual object

When the object reaches at the ZAMS stage, its spectral type and mass can be estimated from the bolometric luminosity. The models of Thompson (1984) and Cox (2000) can be used for the estimation. This is a simple and a relatively reliable method. On the contrary, the mass estimation of the object which is in the pre-main sequence stage is relatively complicated. In this stage, mass accretion is still on-going and a luminosity of a HIYSO or a MYSO is monotonously increasing with time (Hosokawa and Omukai 2009). This indicates that the current luminosity is a lower limit of the final luminosity which will attain at the ZAMS stage. In this study, we estimate the mass of the pre-main sequence object assuming that the object would have had the same luminosity as the present. The estimated mass therefore gives a lower limit of the final mass of the object.

4.1.1 M8E

M8E-radio is considered to be at near the ZAMS stage, because M8E-radio has the UCHII region (Simon et al. 1984). Its spectral type is expected as B2.5-3 by the stellar model of Thompson (1984) using the derived luminosity ($1.5 \pm 0.5 \times 10^3\ L_\odot$) at the assumed distance of 1.5 kpc. This is almost consistent with the estimation of the spectral type of B2 based on the measurement of the free-free emission reported by Simon et al. (1984). The mass is $6.5 \pm 0.5 M_\odot$ using the theoretical models of Cox (2000).

On the contrary, M8E-IR is considered not to reach at the ZAMS stage yet judging from the absence of an UCHII region (Walsh et al. 1998). If its luminosity does not change until reaching at the ZAMS stage, the spectral type of M8E-IR at the ZAMS stage is estimated as B0.5-1 (Thompson 1984). Its mass is estimated as $10.5 \pm 0.5 M_\odot$ using the derived luminosity of $6.5 \pm 0.5 \times 10^3\ L_\odot$ (Cox 2000). These are the lower limits of the spectral type and the mass at the ZAMS stage as mentioned above. The estimated spectral types and masses of M8E-radio and M8E-IR are listed in Table 4.1.

The uncertainty of the distance has also been pointed out to exist in these objects as mentioned in the Chapter 2. However, it is relatively small for the M8E region, from 1.25 to 1.5 kpc. It could change the masses of M8E-radio and M8E-IR to be $5.5 \pm 0.5 M_{\odot}$ and $9.2 \pm 0.2 M_{\odot}$, respectively.

4.1.2 RAFGL 6366S

IR2 has reached at the ZAMS stage due to the existence of the associating UCHII region (Kurtz et al. 1994). Its spectral type is expected as B2.5-3.5 (Thompson 1984) using the derived luminosity ($1.3 \pm 0.4 \times 10^3$ $L_{\odot}$) at the assumed distance of 2.0 kpc. This result gives a good agreement with the estimation of B3 spectral type derived by the measurement of the free-free emission reported by Kurtz et al. (1994). The mass is estimated as $6.5 \pm 0.5 M_{\odot}$ (Cox 2000).

On the other hand, the MYSO in IR1 is considered as a pre-main sequence object because an UCHII region has not been detected in the previous work by Kurtz et al. (1994). If its derived luminosity ($4.8 \pm 1.3 \times 10^3$ $L_{\odot}$) does not change until reaching at the ZAMS stage, the spectral type of IR1 is estimated as B1-1.5 (Thompson 1984). This corresponds to $9.5 \pm 0.5 M_{\odot}$ (Cox 2000). This is the lower limit of the estimation because the MYSO is a pre-main sequence object.

As mentioned in Chapter 2, IR1 consists of the MYSO and the NIR object. The flux contribution of the NIR object is not negligible in the NIR and the short-MIR wavelengths. Rodon (2009) has reported that the NIR flux of IR1 mostly comes from the NIR object. Observations performed in the RMS project (Lumsden et al. 2013) have showed that the MYSO and the NIR object have almost the same luminosities at 11.2 μm. Our 12 μm image also shows an extended structure in IR1. However, such a structure is not seen in our 18 μm image, which suggests that the MYSO dominates the flux of IR1 at 18 μm and longer wavelengths. Even if the MYSO dominates the flux of IR1 only in wavelengths longer than 18 μm, its lower limit of the bolometric luminosity is decreased to be as large as $2.5 \times 10^3 L_{\odot}$ and its ranges of the spectral type and the mass are changed into B1-2.5 and $9 \pm 1 M_{\odot}$, respectively. The estimated spectral types and masses are listed in Table 4.1.

The distance of RAFGL 6366S has large uncertainty up to ±50% (Klein et al. 2005). When the distance is 1.0 kpc, the closest case, the spectral types and masses of IR1 and IR2 are B2.5-4 ($6 \pm 1 M_{\odot}$) and B5-6.5 ($4.5 \pm 0.5 M_{\odot}$), respectively. However, the spectral type of B5-6.5 is too late to form the UCHII region, which is inconsistent with the fact that IR2 has the UCHII region. IR2 should be equal to or earlier than B3 star at the ZAMS stage (Churchwell 2002) and the distance should be equal to or farther than 1.8 kpc. We will adopt this as the closest distance of RAFGL 6366S region in this work. The estimated results at the closest (1.8 kpc) and the farthest (3.0 kpc) cases are also listed in Table 4.1. These results show that their masses do not change largely at any assumed distances.

4.1.3 IRAS 18317-0513

Both IRAS 18317-0513-IR1 and IR2 seem to be pre-main sequence objects (Urquhart et al. 2009). Lower limits of spectral type and mass of IR1 and IR2 are estimated as B1.5-2 ($8.5 \pm 0.5 M_{\odot}$), and B1.5-2.5 ($8 \pm 1 M_{\odot}$), respectively (Thompson 1984; Cox 2000) at the assumed distance of 3.0 kpc. The estimated spectral types and masses are listed in Table 4.1. It includes the estimated spectral types and masses at the closest (2.0 kpc) and the farthest (4.0 kpc) cases.

Table 4.1: The estimated spectral types and masses of objects.

Object	Evolutional stage	Spectral type			Mass ($M_\odot$)		
		Closest	Typical	Farthest	Closest	Typical	Farthest
M8E-IR	MYSO[1]	B1-1.5	B0.5-1	-	9.2 ± 0.2	10.5 ± 0.5	-
M8E-radio	UCHII[2]	B3-4	B2.5-3	-	5.5 ± 0.5	6.5 ± 0.5	-
RAFGL 6366S-IR1	MYSO[1]	B1.5-2.5	B1-2.5	B0.5-1	8 ± 1	9 ± 1	11 ± 1
RAFGL 6366S-IR2	UCHII[2]	B3-4	B2.5-3.5	B1.5-2.5	5.5 ± 0.5	6.5 ± 0.5	8 ± 1
IRAS 18317-0513-IR1	MYSO[1]	B2.5-3	B1.5-2	B1-1.5	6.5 ± 0.5	8.5 ± 0.5	9.5 ± 0.5
IRAS 18317-0513-IR2	MYSO[1]	B2.5-3.5	B1.5-2.5	B1-1.5	6.5 ± 0.5	8 ± 1	9.5 ± 0.5

1: Current spectral types and masses are estimated for the MYSOs.
2: Spectral types and masses are estimated assuming they are at the ZAMS stage for the objects with the UCHIIs.

4.2 Star formation Sequence in each region

It has revealed that the more massive object is at a younger evolutional stage in the M8E and the RAFGL 6366S regions. Since the more massive object generally evolves faster, its formation is expected to have begun after the less massive object had formed. This is consistent with our expected star formation sequence described in Chapter 1. However, it is not clear that the observed sequence remains significant even when taking into account the uncertainty of the mass estimation and other considerable factors. The difference of the ages of the objects might be buried in the uncertainty, or in the worst case, the sequence might be turned over. In this section, we estimate the age of each object and make a quantitative comparison between them.

In general, the star formation timescale is considered to consist of the following two timescales.

1. Timescale of falling self-gravity gas into a central object: $t_{\rm fall}$.
   Classically, this timescale is known as the free-fall timescale assuming the constant gas density. It depends on the gas density and not on the mass of a core or a forming star (Zinnecker and Yorke 2007). The recent model including the realistic density structure and turbulence in the core suggests that the timescale depends on not only a mean gas surface density but also the final mass of the forming star (McKee and Tan 2002). However, the dependence on the final mass of the forming star has been suggested to be weak in this model (McKee and Tan 2002). Therefore, assuming the mean surface density of a typical massive star forming core described in McKee and Tan (2002), we use a value of $1 \times 10^5 yr$ as the gas falling timescale in this study, which is almost constant with the variation of the final mass of the forming star.

2. Timescale of contraction of the central object until it starts hydrogen burning: $t_{\rm KH}$.
   This corresponds to the Kelvin-Helmholtz timescale $t_{\rm KH} \sim G\frac{M_*^2}{R_* L_*}$, where G, M_*, R_*, and L_* represent the gravitational constant and the mass, the radius, and the luminosity of the object. Commonly, $t_{\rm KH}$ gets shorter when the mass gets heavier. Its dependence is evaluated as $t_{\rm KH} \propto M_\star^{-2.2}$ in the mass range of approximately 5 *to* 10 $M_\odot$ based on theoretical simulations (Zinnecker and Yorke 2007; Pietrinferni et al. 2004).

Actually, periods of $t_{\rm fall}$ and $t_{\rm KH}$ during massive star formation may be overlapped because the contraction begins before all the mass infalls (Zinnecker and Yorke 2007). It may make the total timescale shorter than the simple sum of $t_{\rm fall}$ and $t_{\rm KH}$. However, it is very difficult to estimate the overlap exactly. Here, we use the simple sum as the star formation timescale. Figure 4.1 displays a schematic drawing of the star formation timescale.

4.2.1 M8E

In the case of M8E-radio, $t_{\rm KH}$ is estimated as 3 *to* $5 \times 10^5 yr$ from the derived mass of $6.5 \pm 0.5 M_\odot$ (Zinnecker and Yorke 2007). The uncertainty of $t_{\rm KH}$ is caused by the error of the mass estimation. $t_{\rm fall}$ is $1 \times 10^5 yr$. The star formation time scale is 4 *to* $6 \times 10^5 yr$ in total. If M8E-radio is at exactly the ZAMS stage, the age of M8E-radio is equal to this star formation timescale. But it is more likely that M8E-radio spends some time after reaching at the ZAMS stage, and this time should be added to the age. This is expected to be less than the lifetime of the UCHII region, typically $1 \times 10^5 yr$ at most, as shown in Figure 4.2. Therefore, the age of of M8E-radio is 4 *to* $7 \times 10^5 yr$.

On the other hand, $t_{\rm KH}$ of M8E-IR is estimated as $1 \times 10^5 yr$ because its mass is derived as $10.5 \pm 0.5 M_\odot$. With adding $t_{\rm fall}$ of $1 \times 10^5 yr$, the star formation timescale is $2 \times 10^5 yr$ in total. This timescale gives an upper limit of the age of M8E-IR because M8E-IR is the MYSO and

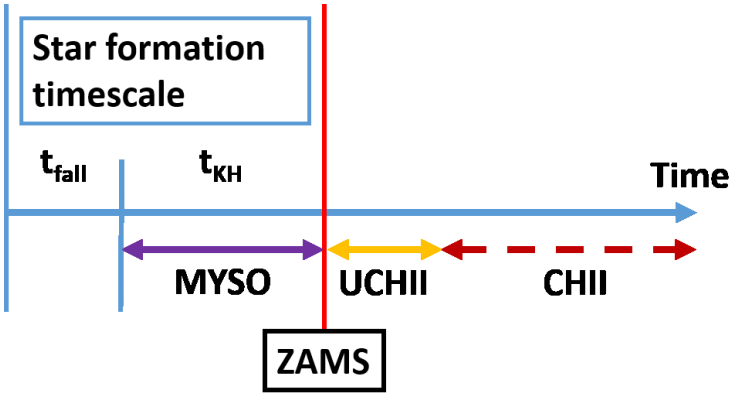

Figure 4.1: The sketch of timescale estimation in this work. The relation between timescales and evolutional stages are shown.

still on its way to the main-sequence stage (see Figure 4.2), i.e., the age of M8E-IR is less than $2 \times 10^5 yr$. Therefore, M8E-IR is younger than M8E-radio by at least $2 \times 10^5 yr$.

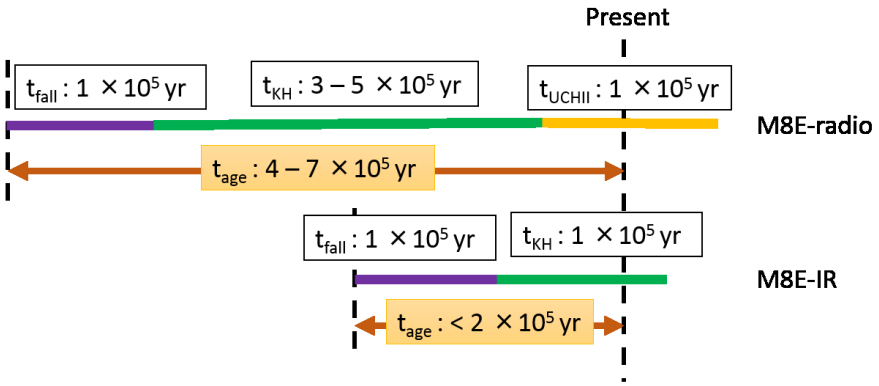

Figure 4.2: The sketch of age estimation of M8E-radio and M8E-IR including the uncertainness of the $t_{\rm KH}$ and evolutional stage of each object. $t_{\rm age}$ represents the age of each object.

However, this age difference could be varied if some uncertainties are taken into account. One possible uncertainty is the estimation of $t_{\rm fall}$. In the above estimations, a constant value of $1 \times 10^5 yr$ was adopted as $t_{\rm fall}$ for the both objects, but it may have weak and positive dependence on the final mass of the objects as discussed above in this section. The massive M8E-IR may have longer $t_{\rm fall}$ than that of M8E-radio and the age difference might become smaller. However, the decrease of the age difference is only $0.2 \times 10^5 yr$ considering that M8E-IR is about twice heavier than M8E-radio.

$t_{\rm fall}$ also negatively depends on the gas density because longer time is necessary for gathering the gas of the stellar mass under lower density condition. If the density of the parental gas which have formed M8E-IR was lower than that of M8E-radio, $t_{\rm fall}$ of M8E-IR would also increase, resulting the age difference might become smaller. It seems inconceivable because the MYSO, such as M8E-IR, is naturally expected to be formed from denser gas. But it is not completely ruled out since the formation of M8E-radio may decrease the density around it due to gathering the gas for forming M8E-radio. Assuming that the variation of the density is expected to be that

of a typical value in massive cores, roughly as large as ±30% (Tan et al. 2014), the difference of $t_{\rm fall}$ is $0.6 \times 10^5 yr$. In total, the age difference might be shortened with $0.8 \times 10^5 yr$ in the worst case. This is significantly shorter than the expected age difference of at least $2 \times 10^5 yr$, which indicates that the uncertainties of $t_{\rm fall}$ do not turn over the star formation sequence.

There is uncertainty in the measurement of the distance to the M8E region, from 1.25 kpc to 1.5 kpc. It might also change the age difference. If the larger distance were adopted, the masses of the both objects would be modified to be larger, hence $t_{\rm KH}$ would become shorter, and the age difference would decrease. However, the distance adopted at present (1.5 kpc) is the farthest case for the M8E region. The age difference is kept constant or slightly increased when the distance of 1.25 kpc is adopted.

4.2.2 RAFGL 6366S

For RAFGL 6366S-IR2, $t_{\rm KH}$ is estimated as 3 *to* $5 \times 10^5 yr$ using the derived mass of $6.5 \pm 0.5 M_\odot$ at the assumed distance of 2.0 kpc. $t_{\rm fall}$ is adopted as $1 \times 10^5 yr$. The star formation timescale is then 4 *to* $6 \times 10^5 yr$ in total. Since RAFGL 6366S-IR2 has the UCHII region, its age is estimated as 4 *to* $7 \times 10^5 yr$ considering the lifetime of the UCHII region.

$t_{\rm KH}$ of RAFGL 6366S-IR1 is estimated as 1 *to* $2 \times 10^5 yr$ from the derived mass of $9 \pm 1 M_\odot$. Adopting the value of $1 \times 10^5 yr$ for $t_{\rm fall}$, the star formation timescale is 2 *to* $3 \times 10^5 yr$ in total. Since this object is in the pre-main sequence stage, its age is 2 *to* $3 \times 10^5 yr$ or shorter. Therefore, the age difference between them is $1 \times 10^5 yr$ or more. This is also longer than the uncertainties of $t_{\rm fall}$ as discussed in the previous subsection.

The distance to the RAFGL 6366S region has not been determined accurately. If the distance of 3.0 kpc is adopted instead of 2.0 kpc, $t_{\rm KH}$ of IR1 and IR2 are varied to $1 \times 10^5 yr$ and 2 *to* $3 \times 10^5 yr$, respectively. Therefore, the age difference still remains $1 \times 10^5 yr$ or more, and it is also longer than the uncertainties of $t_{\rm fall}$.

4.2.3 IRAS 18317-0513

$t_{\rm KH}$ of IRAS 18317-0513-IR1 and IR2 are expected to be almost the same values since their masses are almost the same, $8.5 \pm 0.5 M_\odot$ and $8 \pm 1 M_\odot$, respectively. The star formation timescales and ages of two objects are expected to be almost the same. This conclusion does not change with the uncertainty of the distance because the relative ratio of the luminosities and masses of the two objects does not change when the distance is changed.

The results of the estimation of the star formation timescales and the age differences including $t_{\rm fall}$, $t_{\rm KH}$, and errors of the estimation in the observed regions are listed in Table 4.2.

Table 4.2: The estimated star formation timescales in the observed regions.

Region	Object	Evolutional stage	$t_{\rm fall}$	$t_{\rm KH}$ [1]	The age of object [2]	The age difference
M8E	M8E-IR	MYSO	$\sim 1 \times 10^5 yr$	$1 \times 10^5 yr$	$< 2 \times 10^5 yr$	$> 2^{+0.4}_{-0.8} \times 10^5 yr$
	M8E-radio	UCHII	$\sim 1 \times 10^5 yr$	$3 - 5 \times 10^5 yr$	$4 - 7 \times 10^5 yr$	
RAFGL 6366S	IR1	MYSO	$\sim 1 \times 10^5 yr$	$1 - 2 \times 10^5 yr$	$< 2 - 3 \times 10^5 yr$	$> 1^{+0.4}_{-0.8} \times 10^5 yr$
	IR2	UCHII	$\sim 1 \times 10^5 yr$	$3 - 5 \times 10^5 yr$	$4 - 7 \times 10^5 yr$	
IRAS 18317-0513	IR1	MYSO	$\sim 1 \times 10^5 yr$	$2 \times 10^5 yr$	$< 3 \times 10^5 yr$	-
	IR2	MYSO	$\sim 1 \times 10^5 yr$	$2 - 3 \times 10^5 yr$	$< 3 - 4 \times 10^5 yr$	

1: The result at the assumed distance of a typical value in each region is shown as representative one.
2: Signs of inequality represent ongoing star formation in the MYSOs.

4.2.4 Other massive star forming regions

To confirm whether the expected star formation sequence is universal or not, a literature survey has been carried out. We have searched massive star forming regions 1) which include two or more MYSOs, or more than one MYSO and more than one object with an UCHII region and 2) which have been observed in the multi-wavelengths with sufficient spatial resolution to measure the luminosity of each object. Three regions (Mon R2, ISOSS J18364-0221 SMM1, and AFGL 437) have been selected.

Mon R2

The Mon R2 region is a famous massive star forming region observed well in the multi wavelengths from the NIR to the centimeter wavelengths (de Wit et al. 2009). It includes two massive young stellar objects, IRS1 and IRS3 (Massi et al. 1985). Their separation is about 0.1 pc (de Wit et al. 2009). The mass of IRS1, estimated as $17M_{\odot}$, is heavier than IRS3, estimated as $10M_{\odot}$, (Massi et al. 1985) and an UCHII region is accompanied only with IRS1 (Walsh et al. 1998). These results have represented that the more massive object (IRS1) is more evolved than the less massive object (IRS3). This seemingly appears to be a counter example of the expected star formation sequence.

Since IRS1 is a very heavy object, its $t_{\rm KH}$ is very short. It is estimated as $0.5\times10^5 yr$. Adding the $t_{\rm fall}$ of $1\times10^5 yr$ and the lifetime of the UCHII region, the age of IRS1 is 1.5 *to* $2.5\times10^5 yr$ in total. On the contrary, $t_{\rm KH}$ of IRS3 is $1\times10^5 yr$ and the star formation timescale is $2\times10^5 yr$. This is nearly identical to the age of IRS1 within an error and the ages of IRS1 and IRS3 do not show significant difference quantitatively. It is concluded that the star formation sequence cannot be determined in this region.

ISOSS J18364-0221 SMM1

The ISOSS J18364-0221 SMM1 region is a massive star forming region located in the large star-forming complex ISOSS J18364-0221 with a size of about 100 pc^2 and a mass of about 3200 $M_{\odot}$ (Hennemann et al. 2009). Total gas mass of SMM1 is 75 ± 30 $M_{\odot}$ and its radius is about 0.2 pc (Hennemann et al. 2009). It includes two massive objects called as SMM1 South and SMM1 North with a separation of approximately 0.1 pc (Hennemann et al. 2009). Both objects are MYSOs and not detected at the NIR wavelength (Hennemann et al. 2009). SED fittings from the MIR to the millimeter wavelengths have revealed the effective temperatures of SMM1 South and SMM1 North are 22 K and 15 K, respectively. The mass of SMM1 South is estimated as $12M_{\odot}$ and that of SMM1 North as $18M_{\odot}$ (Hennemann et al. 2009). SMM1 South is very bright at 24 μm, associated with jet, and has turbulent central region traced by HCN(1-0) observations (Hennemann et al. 2009). All these observational results suggest that SMM1 South is a typical MYSO. On the other hand, SMM1 North is not detected at 24 μm and not associated with jet or turbulence(Hennemann et al. 2009). These imply that SMM1 North is relatively quiescent object and seems to be before or the very early phase of the accretion and the contraction phase. The less massive object, SMM1 South, is at a more evolved phase than the more massive object, SMM1 North. This suggests that the less massive SMM1 South has formed earlier than the more massive SMM1 North in this region although no UCHII regions have been detected there. This region could be at a more previous phase than the M8E and the RAFGL 6366S regions.

AFGL 437

The AFGL 437 region is a compact and clustering massive star forming region containing a few dozen NIR objects. At the MIR wavelengths, four objects, AFGL 437W, AFGL 437S, AFGL 437N, and WK34 are very prominent (de Wit et al. 2009; Kumar Dewangan and Anandarao 2010). All the objects are distributed within about 0.15 pc (de Wit et al. 2009). AFGL 437W and AFGL 437S associate with UCHII regions while the other two do not (Kumar Dewangan and Anandarao 2010). The masses of AFGL 437W, AFGL 437S, AFGL 437N, and WK34 have been estimated to be $8M_{\odot}$, $8M_{\odot}$, $9M_{\odot}$, and $7M_{\odot}$, respectively (Kumar Dewangan and Anandarao 2010). All the reported masses of the four objects are almost the same and this region is not applicable for further discussion of the star formation sequence because their ages are also estimated as almost the same values.

Relation between star formation sequences and projected spatial scales?

Star formation sequences and projected spatial scales obtained in the literature search are summarized in Table 4.3. Although the projected spatial scales of the literature-searched regions are relatively larger than our observed regions, the derived star formation sequences do not seem to depend on the projected spatial scales.

Table 4.3: Massive Star Forming Region and Their Property

Object region	Distance [kpc]	Spatial scale [pc]	Mass of object with UCHII	Mass of MYSO	Star formation sequence	Reference
Mon R2	0.83	0.1	$17M_{\odot}$	$10M_{\odot}$	MYSO $\Rightarrow$ HIYSO[2]	1,2
ISOSS J18364-0221 SMM1	2.2	0.1	-	$18M_{\odot}$[1],$12M_{\odot}$	HIYSO $\Rightarrow$ MYSO	3
AFGL 437	2.7	0.15	$8M_{\odot}$,$8M_{\odot}$	$9M_{\odot}$,$7M_{\odot}$	-	1,4
M8E	1.5	0.05	$6.5 \pm 0.5M_{\odot}$	$10.5 \pm 0.5M_{\odot}$	HIYSO $\Rightarrow$ MYSO	This Work
RAFGL 6366S	2.0	0.07	$6.5 \pm 0.5M_{\odot}$	$9 \pm 1M_{\odot}$	HIYSO $\Rightarrow$ MYSO	This Work
IRAS 18317-0513	3.0	0.07	-	$8.5 \pm 0.5M_{\odot}$,$8 \pm 1M_{\odot}$	-	This Work

[1] Represents the youngest object among MYSOs.
[2] Apparently seemed sequence. Note that the age estimation suggests no significant age difference between IRS1 and IRS3.
(1) de Wit et al. (2009); (2) Massi et al. (1985); (3) Hennemann et al. (2009); (4) Kumar Dewangan and Anandarao (2010)

4.3 Summary of the study of the star formation sequences

The masses and the evolutional stages of the objects in our observed and literature-searched regions are summarized in Figure 4.3. In three regions, the HIYSOs have formed earlier than the MYSOs, which gives good agreements with our expectation discussed in Chapter 1. In another two regions, whether the HIYSOs have formed earlier or not cannot be discussed because all the objects have almost the same masses. In the Mon R2 region, the detailed age estimation has shown that which object has formed earlier cannot be determined due to their relatively heavy masses. Although the number of the studied regions is not enough for detailed statistical evaluation, the results have shown that some of the observed regions show the star formation sequences which is consistent with our expected ones.

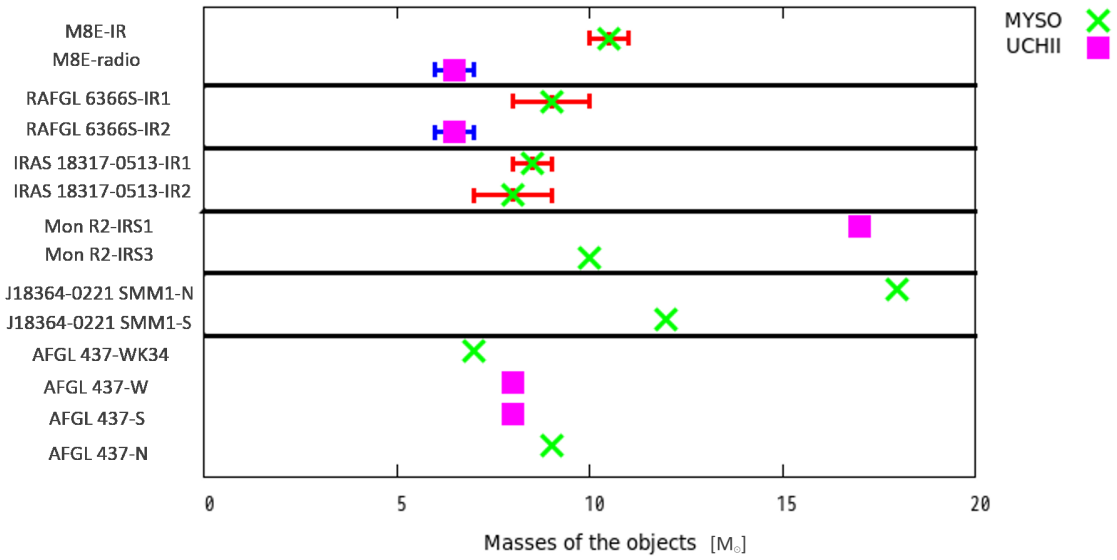

Figure 4.3: The summary of the masses and the evolutional stages of the objects in the all regions. The error of the masses are also represented in our observed regions.

Chapter 5

Model estimation of radiative heating effect

5.1 Quantitative Evaluation of radiative heating by the HIYSO

In the previous chapter, we have suggested that the HIYSOs had existed before the formation of the MYSOs. However, it is not clear that radiative energy from the HIYSO is enough for heating a cloud to the temperature required to physically support the massive CC. In this section, we will estimate the gas temperature around the HIYSO under simple assumptions. The M8E region is focused on as a typical case.

5.1.1 Temperature structure made from radiative heating

We assume that the cloud has constant density and contains a single HIYSO in the pre-main sequence stage as shown in Figure 5.1. In this stage, the HIYSO is deeply embedded in the dense envelope and its radiation can be considered as a blackbody at the temperature of the envelope, approximately 100 K (Kurtz et al. 2000; Churchwell 2002; Sridharan et al. 2002). The density of a typical value of IRDCs, $n_{H_2} \sim 10^4\ cm^{-3}$ (Longmore et al. 2011), is adopted as that of the cloud. This corresponds to an optical depth of $A_v \sim 6\ mag$ with a size of 0.1 pc. It is sufficiently transparent for the radiation from the envelope containing the HIYSO and therefore we can treat this as an optical thin condition.

A temperature of a dust particle at a radius of r from the HIYSO is determined by the radiation equilibrium between the radiative heating by the HIYSO and re-emitting from the dust particle itself, as the following equation,

$$\int \frac{4\pi r_{HIYSO}^2}{4\pi r^2} \pi a^2 \varepsilon(\lambda) F_{HIYSO}(\lambda) d\lambda = \int 4\pi a^2 \varepsilon(\lambda) F_{dust}(\lambda, r) d\lambda, \tag{5.1}$$

where $r_{HIYSO}, a, \varepsilon(\lambda), F_{HIYSO}(\lambda), and\ F_{dust}(\lambda, r)$ represent the radius of the circumstellar envelope accompanied with the HIYSO, the radius of the dust particle, the dust emissivity, spectral intensity from the HIYSO with the circumstellar envelope, and spectral intensity of the re-emission from the dust particle. Here, the re-emission from the dust particle is considered as modified black body radiation with the dust emissivity, $\varepsilon(\lambda) \sim \lambda^{-\beta}$. An absorption coefficient of the dust particle is also represented as $\varepsilon(\lambda)$. The equation of the radiation equilibrium is rewritten as the following,

$$\int \frac{4\pi r_{HIYSO}^2}{4\pi r^2} \pi a^2 \varepsilon(\lambda) B_\lambda(T_{HIYSO}) d\lambda = \int 4\pi a^2 \varepsilon(\lambda) B_\lambda(T_{dust}(r)) d\lambda, \tag{5.2}$$

where $B_\lambda(T), T_{HIYSO}, and\ T_{dust}(r)$ represent the black body radiation of a certain temperature T, the effective temperature of the HIYSO with the envelope, and the temperature of the dust particle at the radius of r from the HIYSO. Therefore, $T_{dust}(r)$ is,

$$T_{dust}(r) = T_{HIYSO}\left(\frac{r_{HIYSO}^2}{4r^2}\right)^{\frac{1}{4+\beta}} = T_{HIYSO}^{\frac{\beta}{4+\beta}}\left(\frac{L_{HIYSO}}{16\pi\sigma r^2}\right)^{\frac{1}{4+\beta}}, \tag{5.3}$$

where $L_{HIYSO}\ and\ \sigma$ represent the luminosity of the HIYSO and the Stefan-Boltzmann constant. Here, r_{HIYSO} is converted to L_{HIYSO} as the following equation,

$$L_{HIYSO} = 4\pi r_{HIYSO}^2 \sigma T_{HIYSO}^4. \tag{5.4}$$

When the density of the dust and the gas is relatively high, it is naturally expected the dust temperature is equal to the gas temperature. Then, the gas temperature at the radius of r from the HIYSO, $T_{gas}(r)$, is,

$$T_{gas}(r) = T_{dust}(r) = T_{HIYSO}^{\frac{\beta}{4+\beta}}\left(\frac{L_{HIYSO}}{16\pi\sigma r^2}\right)^{\frac{1}{4+\beta}}. \tag{5.5}$$

In this estimation, the dust emissivity index, β, is assumed as 2, which is a typical observed value in massive star forming regions (Hill et al. 2006).

We consider the case of the M8E region. In order to form the object with the mass of 10.5 $M_\odot$, corresponding to M8E-IR, the gas temperature should be higher than 48 K derived from the equation of the Jeans mass. A typical temperature of the HIYSO is considered as 100 K (Grave and Kumar 2009; Sridharan et al. 2002). The luminosity of M8E-radio is measured as 1.5×10^3 $L_\odot$ in this work, but the luminosity in the pre-main sequence stage is considered to be lower (Hosokawa and Omukai 2009; Zinnecker and Yorke 2007; Palla and Stahler 1993). Therefore, we first adopt the luminosity of 900 $L_\odot$ in this calculation. This is the luminosity of the HIYSO with a mass of 6.5 $M_\odot$, corresponding to M8E-radio, at the birth line expected by the stellar model of Siess et al. (2000). The result of calculation is shown in Figure 5.2. The temperature at 0.05 pc, where M8E-IR is located, in this case is some what lower, 29 K, than required one. However, $T_{gas}(r)$ strongly depends on input parameters, T_{HIYSO} and L_{HIYSO}. According to observations by such as Grave and Kumar (2009), Kurtz et al. (2000), and Sridharan et al. (2002), T_{HIYSO} may vary in a range from 50 K to 200 K. L_{HIYSO} may also vary when the accretion rate of the HIYSO varies because the luminosity is roughly proportional to the accretion rate in the pre-main sequence stage. Assuming that the accretion rate may change as large as one order of magnitude from a typical value during star formation, L_{HIYSO} changes in a range from 100 $L_\odot$ to 4000 $L_\odot$ (Krumholz 2006; Krumholz et al. 2007; Hosokawa and Omukai 2009). When T_{HIYSO} is 200 K and L_{HIYSO} is 4000 $L_\odot$, $T_{gas}(r)$ at 0.05 pc is estimated as 46 K as shown in Figure 5.2. In this case, the Jeans mass becomes 10 $M_\odot$ which almost corresponds to the derived mass of M8E-IR within the error (10.5 ± 0.5 $M_\odot$).

It is notable that the gas temperature of the M8E region is measured as 30 to 40 K by CO observations with a beam size of 0.2 pc (Tothill et al. 2002). This is roughly consistent with or slightly higher than our calculation. However, the gas temperature at present would correspond to the temperature of the already formed massive core, not the previously existing cloud, and it may also be affected by additional radiation from M8E-IR at present.

5.1.2 Collapsing mass estimation of heated gas

In addition to the gas temperature, it should be considered whether a collapsing mass of a CC in the heated gas is large enough for forming the MYSO or not. The collapsing mass of the

CC in the heated gas is estimated from the Jeans mass. Of course the Jeans mass is defined under isothermal condition in a strict sense, but we adopt a mean temperature, $\bar{T}_{gas}(R)$, instead because the cloud has temperature structure. This is a volume averaged temperature within the radius of R from the HIYSO described as following,

$$\bar{T}_{gas}(R) = \frac{1}{\frac{4\pi R^3}{3}} \int_0^R T_{dust}(r') 4\pi r'^2 dr' = \frac{12+3\beta}{10+3\beta} T_{dust}(R) = \frac{9}{8} T_{dust}(R). \tag{5.6}$$

In this case, the Jeans mass is expressed as,

$$M_{collap} = M_J = 1.7 \times 10^{-10} \bar{T}_{gas}(R_{collap})^{\frac{3}{2}} \rho^{-\frac{1}{2}} [M_\odot], \tag{5.7}$$

where M_{collap}, M_J, R_{collap}, and ρ represent the collapsing mass, the Jeans mass, the radius of the collapsing region from the HIYSO, and the gas density as shown in Figure 5.3. Because the constant gas density is assumed in this model (see Figure 5.3), M_{collap} is also written as,

$$M_{collap} = \rho \frac{4\pi R_{collap}^3}{3}. \tag{5.8}$$

Using the above two equations, the equation of the collapsing mass can be described without R_{collap},

$$M_{collap} = 4.8 \times 10^{-10} \rho^{-\frac{2}{7}} T_{HIYSO}^{\frac{3}{7}} L_{HIYSO}^{\frac{3}{14}} [M_\odot]. \tag{5.9}$$

As compared with the original equation of the Jeans mass, dependence of the collapsing mass on the density decreases.

When ρ of 3×10^{-17} kg m^{-3}, corresponding to $n_{H_2} \sim 10^4$ cm^{-3}, T_{HIYSO} of 100 K, and L_{HIYSO} of 900 $L_\odot$ are substituted for the case of the M8E region, M_{collap} is derived to be 4 $M_\odot$. M_{collap} may be increased up to 8 $M_\odot$ if T_{HIYSO} is 200 K and L_{HIYSO} is 4000 $L_\odot$ in the same manner as the previous subsection. This is not sufficient for the mass of M8E-IR, 10.5 $M_\odot$, but gives an agreement within a factor of 1.5. In this case, $\bar{T}_{gas}(R_{collap})$ is 36 K and R_{collap} is 0.15 pc.

The luminosity may be further increased by the contribution of lower-mass YSOs coexisting around the HIYSO. Each of YSOs is not so luminous compared to the HIYSO, but they are abundant. If the mass function of YSO is given by the Salpeter's IMF law (Salpeter 1955) and each YSO has a luminosity at its birth line (Siess et al. 2000), the whole luminosity of the lower-mass YSOs is twice larger than that of the single HIYSO, which increases M_{collap} by 30 %. Note that this gives an upper limit because a luminosity of a lower-mass YSO becomes the maximum value at the birth line and drastically decreases during the pre-main sequence stage (Palla and Stahler 1993). Detailed evolutional models and information of ages of the lower-mass YSOs are required to estimate the actual contribution of the lower-mass YSOs exactly. This is out of scope of this simple calculation discussed here.

In conclusion, our calculation has demonstrated that the collapsing mass of the CC may be increased up to near the mass of the MYSO (M8E-IR) if the luminosity of the HIYSO (and the lower-mass YSOs) is large enough. The expected collapsing mass gives an agreement with the mass of the MYSO within a factor of 1.5. This is the case of the M8E region, and similar results are obtained for the other two regions, the RAFGL 6366S and the ISOSS J18364-0221 SMM1 regions. For further discussions, detailed theoretical models of the radiative heating in the IRDCs which include gas density structure, an effect of the turbulence, and the stellar evolution of the lower-mass YSOs are needed in addition to detailed observations.

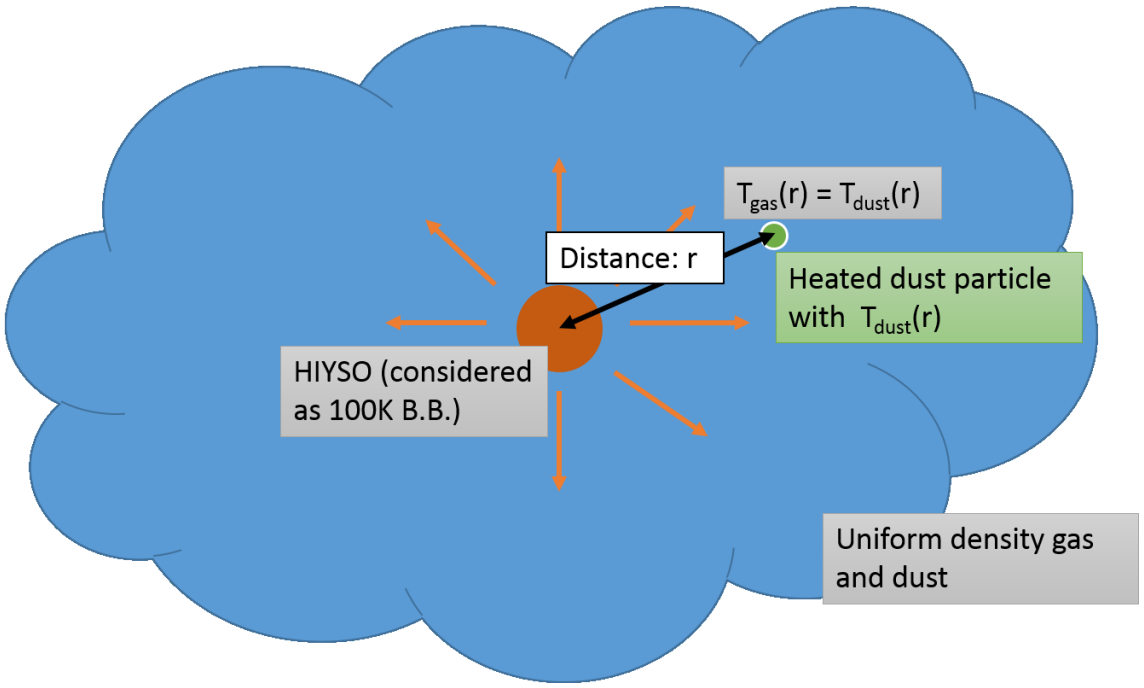

Figure 5.1: The sketch of the model as described in the section 5.1.1. The HIYSO heats up the surrounding dust particles and molecular gas. The uniform dust and gas density is assumed here.

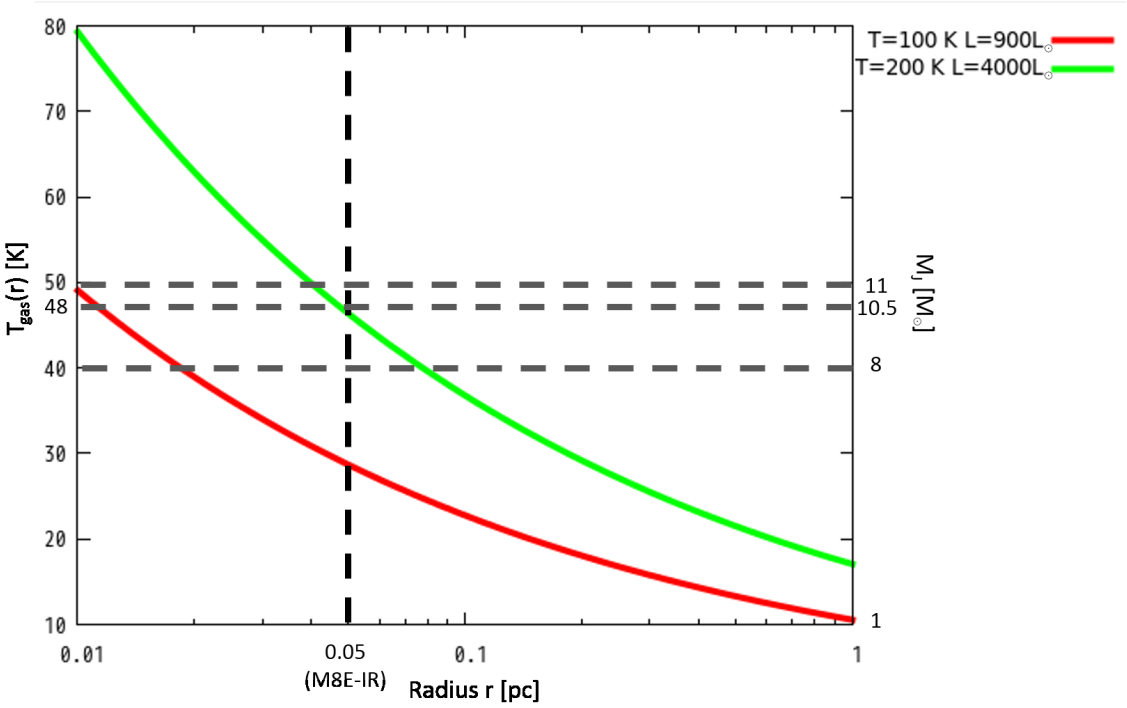

Figure 5.2: The decrement of gas temperature with the change of radius. The Jeans mass corresponds to the gas temperature is also represented. The case of when T_{HIYSO} is 200 K and L_{HIYSO} is 4000 $L_\odot$ and the typical case (T_{HIYSO} is 100 K and L_{HIYSO} is 900 $L_\odot$) are plotted.

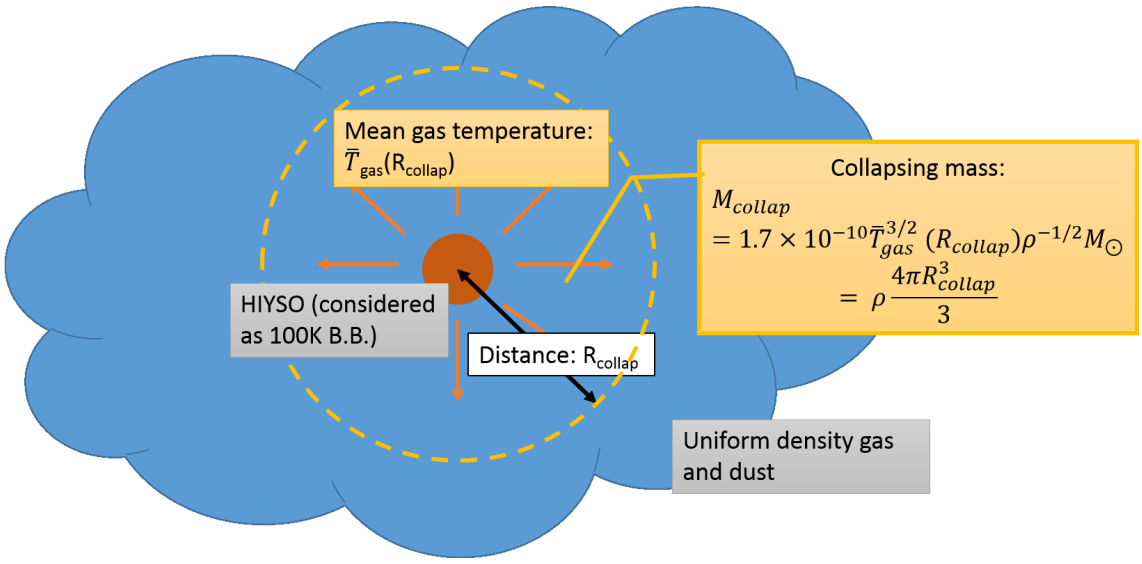

Figure 5.3: The sketch of the collapsing mass evaluation. The mass is assumed as the Jeans mass of the mean temperature of the gas.

Chapter 6

Conclusion and Future work

In this work, three massive star forming regions, the M8E, the RAFGL 6366S, and the IRAS 18317-0513 regions, have been observed in the mid-infrared wavelengths, including 31- and 37-micron bands, to examine the star formation sequences between HIYSOs and MYSOs. Our developed mid-infrared camera MAX38 mounted on the miniTAO telescope has been used for this study. The observations have brought us the first images of these regions at longer than 30-microns from ground. The spatial resolution in our observations achieves approximately 8 arcsec at 31 microns and 9 arcsec at 37 microns which is the highest resolution among the other observations carried out so far. Images of all these 0.1-pc size regions, which have achieved enough high spatial resolution to resolve individual objects, have been successfully obtained. These images have enabled us to measure an infrared luminosity of each object separately.

Individual spectral type and stellar mass have been estimated from the derived luminosities using a stellar model. In the M8E and RAFGL 6366S regions, it has been found that the objects associated with the UCHII regions have relatively lower masses than the other objects. Because less massive YSOs are expected to have longer star formation timescales, they may form earlier and more massive objects latter. These star formation sequences have also been confirmed by a quantitative age estimation of each object. Furthermore, a literature survey has been carried out to extend the number of samples. The similar star formation sequence has also been found in one region out of three. In total, such sequences have been confirmed in three out of six regions and the same star formation sequences could have not been ruled out in the other three regions. This suggests that the radiative heating by the previously formed HIYSO helps the formation of MYSO in the massive star forming regions.

Furthermore, we have estimated the gas temperature and the mass of the CC in the heated gas using a simple cloud model under assumption of dust thermal equilibrium. It has been suggested that the radiative heating by the HIYSO can increase the gas temperature enough to form the MYSO in a certain case within a possible range of a luminosity and a temperature of the HIYSO. It has also been suggested that the increased mass of the CC, assuming that it is equal to the Jeans mass, from the radiative heating by the HIYSO almost corresponds to the mass of the MYSO in a certain case.

This work may provide the first observational evidence that the radiative heating by the previously formed HIYSO induces the formation of the MYSO. This result also suggests speculation that masses of newly formed YSOs in the IRDCs always increase from the first-formed low-mass YSOs to finally-formed MYSOs due to the radiative heating by the previously formed YSOs in the IRDCs. Detailed theoretical models of the radiative heating in the IRDCs will give further information of the star formation sequences between HIYSOs and MYSOs and the effect of the radiative heating by the HIYSO.

Furthermore, more extensive observations of 0.1-pc size massive star forming regions including the long-MIR are strictly needed to check the universality of this star formation sequence between the HIYSO and the MYSO. Such observations will be able to be largely carried out in the near future using the developing telescope and instruments, i.e., the MIR camera MIMIZUKU mounted on TAO 6.5-m telescope (Kamizuka et al. 2014; Yoshii et al. 2014). When observations using the TAO/MIMIZUKU will be available, the sensitivity in the long-MIR is about 40 times as good as observations using the miniTAO/MAX38 and the spatial resolution is 6.5 times as high as those. (Kamizuka et al. 2014). These mean that HIYSOs and MYSOs which are as faint as 1 Jy at 30 micron can be observed and their separations are as small as 1 arcsec can be resolved at 30 micron in massive star forming regions with the TAO/MIMIZUKU. Considering these improvements, observations with the TAO/MIMIZUKU will enable us to study more than 20 additional massive star forming regions, which is estimated from fluxes of HIYSOs and MYSOs and crowdedness of massive star forming regions in the catalog of the RMS project (Lumsden et al. 2013). Such a future large survey will bring us further information of the star formation sequences between HIYSOs and MYSOs. They may also reveal us the universality of such star formation sequences with more extended mass ranges, including intermediate mass objects with masses of 2 *to* 5 $M_{\odot}$, due to improvement of the sensitivity in the long-MIR.

Acknowledgment

I would like to express my gratitude to Assoc. Prof. Takashi Miyata for the leadership and teaching me. Also, I greatly appreciate the feedback offered by Assitant Prof. Shigeyuki Sako. Without their guidance and persistent help, this thesis would not have been able to accomplish.

I want to thank the members of my laboratory; Dr. Takafumi Kamizuka, Dr. Ryo Ohsawa, Dr. Kentaro Asano, Mr. Kazushi Okada, Mr. Masahito Uchiyama, and Mr. Kiyoshi Mouri. Prof. Takuya Yamashita has given me insightful discussion, comments, and suggestions. Dr. Takuya Fujiyoshi has also given me constructive comments. I appreciate their kindness.

I received generous support from the miniTAO/TAO project members for carrying out the MAX38 observations. I especially would like to thank for support from the ANIR/SWIMS members, Assoc. Prof. Kentaro Motohara, Assitant Prof. Masahiro Konishi, Dr. Hidenori Takahashi, Mrs. Natsuko Mitani Kato, Mr. Yutaro Kitagawa, Mr. Soya Todo, and Mr. Yutaka Koboyakawa, for the miniTAO operations and scientific discussion and encouragement.

This work has been supported by the Grant-in-Aid for Scientific Research (26·0274) from the JSPS and Optical and Near-Infrared Astronomy Inter-University Cooperation Program from the MEXT.

This thesis has made use of information from the Red MSX Source survey database[1] which was constructed with support from the Science and Technology Facilities Council of the UK. I also thank to it.

This thesis has made use of analysis tools from the tasks of IRAF. IRAF is distributed by the National Optical Astronomy Observatory, which is operated by the Association of Universities for Research in Astronomy (AURA) under cooperative agreement with the National Science Foundation. I want to thank to it.

My colleague's, Dr. Ken Tateuchi, Dr. Satoshi Hamano, Dr. Hideki Umehata, and Mr. Hirokazu Fujii, give me great encouragement. I would like to express my gratitude to my families and dearly beloved for supporting and encouraging me during my long grad-student life.

[1] http://rms.leeds.ac.uk/cgi-bin/public/RMS_DATABASE.cgi

References

J. I. Arias, R. H. Barbá, and N. I. Morrell. Pre-main-sequence stars in the Lagoon Nebula (M8). *MNRAS*, 374:1253–1263, February 2007.

K. Asano. 地上 30um 帯観測手法の開発、及び惑星状星雲 NGC6302 の観測. Master's thesis, Institute of Astronomy, School of science, the University of Tokyo, Tokyo, Japan, January 2011.

K. Asano, T. Miyata, S. Sako, T. Kamizuka, T. Nakamura, M. Uchiyama, M. Yoneda, H. Kataza, Y. Yoshii, M. Doi, K. Kohno, K. Kawara, M. Tanaka, K. Motohara, T. Tanabe, T. Minezaki, T. Morokuma, Y. Tamura, T. Aoki, T. Soyano, K. Tarusawa, N. Kato, M. Konishi, S. Koshida, H. Takahashi, T. Handa, and K. Tateuchi. Perfomance verification of the ground-based mid-infrared camera MAX38 on the MiniTAO Telescope. In *Society of Photo-Optical Instrumentation Engineers (SPIE) Conference Series*, volume 8446 of *Society of Photo-Optical Instrumentation Engineers (SPIE) Conference Series*, September 2012.

H. Beuther, J. Tackenberg, H. Linz, T. Henning, O. Krause, S. Ragan, M. Nielbock, R. Launhardt, A. Schmiedeke, F. Schuller, P. Carlhoff, Q. Nguyen-Luong, and T. Sakai. The onset of high-mass star formation in the direct vicinity of the Galactic mini-starburst W43. *A&A*, 538: A11, February 2012.

J. M. Carpenter, R. L. Snell, and F. P. Schloerb. Anatomy of the Gemini OB1 molecular cloud complex. *ApJ*, 445:246–268, May 1995.

E. Churchwell. Ultra-Compact HII Regions and Massive Star Formation. *ARA&A*, 40:27–62, 2002.

M. Cohen, R. G. Walker, B. Carter, P. Hammersley, M. Kidger, and K. Noguchi. Spectral Irradiance Calibration in the Infrared. X. A Self-Consistent Radiometric All-Sky Network of Absolutely Calibrated Stellar Spectra. *AJ*, 117:1864–1889, April 1999.

H. D. B. Cooper, S. L. Lumsden, R. D. Oudmaijer, M. G. Hoare, A. J. Clarke, J. S. Urquhart, J. C. Mottram, T. J. T. Moore, and B. Davies. The RMS survey: near-IR spectroscopy of massive young stellar objects. *MNRAS*, 430:1125–1157, April 2013.

A. N. Cox. *Allen's astrophysical quantities*. 2000.

R. M. Crutcher. Magnetic Fields in Molecular Clouds. *ARA&A*, 50:29–63, September 2012.

R. M. Crutcher, B. Wandelt, C. Heiles, E. Falgarone, and T. H. Troland. Magnetic Fields in Interstellar Clouds from Zeeman Observations: Inference of Total Field Strengths by Bayesian Analysis. *ApJ*, 725:466–479, December 2010.

J. M. De Buizer, M. R. Morris, E. E. Becklin, H. Zinnecker, T. L. Herter, J. D. Adams, R. Y. Shuping, and W. D. Vacca. First Science Observations with SOFIA/FORCAST: 6-37 μm Imaging of Orion BN/KL. *ApJ*, 749:L23, April 2012.

W. J. de Wit, M. G. Hoare, T. Fujiyoshi, R. D. Oudmaijer, M. Honda, H. Kataza, T. Miyata, Y. K. Okamoto, T. Onaka, S. Sako, and T. Yamashita. Resolved 24.5 micron emission from massive young stellar objects. *A&A*, 494:157–178, January 2009.

B. T. Draine. *Physics of the Interstellar and Intergalactic Medium.* Princeton University Press, ISBN: 978-0-691-12214-4, 2011.

M. K. Dunham, E. Rosolowsky, N. J. Evans, II, C. J. Cyganowski, J. Aguirre, J. Bally, C. Battersby, E. T. Bradley, D. Dowell, M. Drosback, A. Ginsburg, J. Glenn, P. Harvey, M. Merello, W. Schlingman, Y. L. Shirley, G. S. Stringfellow, J. Walawender, and J. P. Williams. The Bolocam Galactic Plane Survey. III. Characterizing Physical Properties of Massive Star-forming Regions in the Gemini OB1 Molecular Cloud. *ApJ*, 717:1157, July 2010.

S. Faúndez, L. Bronfman, G. Garay, R. Chini, L.-Å. Nyman, and J. May. SIMBA survey of southern high-mass star forming regions. I. Physical parameters of the 1.2 mm/IRAS sources. *A&A*, 426:97–103, October 2004.

J. M. C. Grave and M. S. N. Kumar. Spitzer-IRAC GLIMPSE of high mass protostellar objects. II. SED modelling of a bona fide sample. *A&A*, 498:147–159, April 2009.

M. G. Hauser, T. Kelsall, S. H. Moseley, Jr., R. F. Silverberg, T. Murdock, G. Toller, W. Spiesman, and J. Weiland. The diffuse infrared background - COBE and other observations. In S. S. Holt, C. L. Bennett, and V. Trimble, editors, *After the first three minutes*, volume 222 of *American Institute of Physics Conference Series*, pages 161–178, April 1991.

M. Hennemann, S. M. Birkmann, O. Krause, D. Lemke, Y. Pavlyuchenkov, S. More, and T. Henning. Star-Forming Cores Embedded in a Massive Cold Clump: Fragmentation, Collapse, and Energetic Outflows. *ApJ*, 693:1379–1391, March 2009.

T. Hill, M. A. Thompson, M. G. Burton, A. J. Walsh, V. Minier, M. R. Cunningham, and D. Pierce-Price. Millimetre continuum observations of southern massive star formation regions - II. SCUBA observations of cold cores and the dust grain emissivity index (β). *MNRAS*, 368: 1223–1268, May 2006.

T. Hosokawa and K. Omukai. Evolution of Massive Protostars with High Accretion Rates. *ApJ*, 691:823–846, January 2009.

T. Kamizuka, T. Miyata, S. Sako, R. Ohsawa, K. Asano, M. Uchiyama, K. Okada, M. Uchiyama, T. Nakamura, I. Sakon, T. Onaka, H. Kataza, T. Aoki, M. Doi, N. M. Kato, K. Kawara, Y. Kitagawa, K. Kohno, M. Konishi, S. Koshida, T. Minezaki, T. Morokuma, K. Motohara, T. Soyano, H. Takahashi, Y. Tamura, T. Tanabé, M. Tanaka, K. Tarusawa, K. Tateuchi, S. Todo, and Y. Yoshii. Revised specifications and current development status of MIMIZUKU: the mid-infrared instrument for the TAO 6.5-m telescope. In *Society of Photo-Optical Instrumentation Engineers (SPIE) Conference Series*, volume 9147 of *Society of Photo-Optical Instrumentation Engineers (SPIE) Conference Series*, page 3, July 2014.

A. Kawamura, T. Onishi, Y. Yonekura, K. Dobashi, A. Mizuno, H. Ogawa, and Y. Fukui. A ^{13}CO Survey of Molecular Clouds in Gemini and Auriga. *ApJS*, 117:387–425, July 1998.

R. Klein, B. Posselt, K. Schreyer, J. Forbrich, and T. Henning. A Millimeter Continuum Survey for Massive Protoclusters in the Outer Galaxy. *ApJS*, 161:361–393, December 2005.

M. R. Krumholz. Radiation Feedback and Fragmentation in Massive Protostellar Cores. *ApJ*, 641:L45–L48, April 2006.

M. R. Krumholz, R. I. Klein, and C. F. McKee. Radiation-Hydrodynamic Simulations of Collapse and Fragmentation in Massive Protostellar Cores. *ApJ*, 656:959–979, February 2007.

L. Kumar Dewangan and B. G. Anandarao. Spitzer IRAC imaging photometric study of the massive star-forming region AFGL 437. *MNRAS*, 402:2583–2590, March 2010.

S. Kurtz, E. Churchwell, and D. O. S. Wood. Ultracompact H II regions. 2: New high-resolution radio images. *ApJS*, 91:659–712, April 1994.

S. Kurtz, R. Cesaroni, E. Churchwell, P. Hofner, and C. M. Walmsley. Hot Molecular Cores and the Earliest Phases of High-Mass Star Formation. *Protostars and Planets IV*, pages 299–326, May 2000.

H. Linz, T. Henning, M. Feldt, I. Pascucci, R. van Boekel, A. Men'shchikov, B. Stecklum, O. Chesneau, T. Ratzka, S. P. Quanz, C. Leinert, L. B. F. M. Waters, and H. Zinnecker. Mid-infrared interferometry of massive young stellar objects. I. VLTI and Subaru observations of the enigmatic object M8E-IR. *A&A*, 505:655–661, October 2009.

S. N. Longmore, T. Pillai, E. Keto, Q. Zhang, and K. Qiu. Is Protostellar Heating Sufficient to Halt Fragmentation? A Case Study of the Massive Protocluster G8.68-0.37. *ApJ*, 726:97, January 2011.

A. López-Sepulcre, R. Cesaroni, and C. M. Walmsley. A comparative study of high-mass cluster forming clumps. *A&A*, 517:A66, July 2010.

A. López-Sepulcre, C. M. Walmsley, R. Cesaroni, C. Codella, F. Schuller, L. Bronfman, S. J. Carey, K. M. Menten, S. Molinari, and A. Noriega-Crespo. SiO outflows in high-mass star forming regions: A potential chemical clock? *A&A*, 526:L2, February 2011.

S. D. Lord. A new software tool for computing Earth's atmospheric transmission of near- and far-infrared radiation. Technical report, December 1992.

S. L. Lumsden, M. G. Hoare, J. S. Urquhart, R. D. Oudmaijer, B. Davies, J. C. Mottram, H. D. B. Cooper, and T. J. T. Moore. The Red MSX Source Survey: The Massive Young Stellar Population of Our Galaxy. *ApJS*, 208:11, September 2013.

M.-M. Mac Low and R. S. Klessen. Control of star formation by supersonic turbulence. *Reviews of Modern Physics*, 76:125–194, January 2004.

M. Marseille, S. Bontemps, F. Herpin, F. F. S. van der Tak, and C. R. Purcell. Evolution of massive protostars: the IRAS 18151-1208 region. *A&A*, 488:579–595, September 2008.

M. Massi, M. Felli, and M. Simon. Radio continuum observations of the blister type H II region in MON R2. *A&A*, 152:387–392, November 1985.

C. F. McKee and J. C. Tan. Massive star formation in 100,000 years from turbulent and pressurized molecular clouds. *Nature*, 416:59–61, March 2002.

P. G. Mezger, W. Altenhoff, J. Schraml, B. F. Burke, E. C. Reifenstein, III, and T. L. Wilson. A New Class of Compact H II Regions Associated with OH Emission Sources. *ApJ*, 150:L157, December 1967.

T. Minezaki, D. Kato, S. Sako, M. Konishi, S. Koshida, N. Mitani, T. Aoki, M. Doi, T. Handa, Y. Ita, K. Kawara, K. Kohno, T. Miyata, K. Motohara, T. Soyano, T. Tanabé, M. Tanaka, K. Tarusawa, Y. Yoshii, L. Bronfman, M. T. Ruiz, and M. Hamuy. The University of Tokyo Atacama 1.0-m Telescope. In *Society of Photo-Optical Instrumentation Engineers (SPIE) Conference Series*, volume 7733 of *Society of Photo-Optical Instrumentation Engineers (SPIE) Conference Series*, July 2010.

T. Miyata, S. Sako, T. Kamizuka, T. Nakamura, K. Asano, M. Uchiyama, M. Konishi, M. Yoneda, N. Takato, Y. Yoshii, M. Doi, K. Kohno, K. Kawara, M. Tanaka, K. Motohara, T. Minezaki, T. Tanabe, T. Morokuma, Y. Tamura, T. Aoki, T. Soyano, K. Tarusawa, H. Takahashi, S. Koshida, and N. M. Kato. Evaluations of new atmospheric windows at thirty micron wavelengths for astronomy. In *Society of Photo-Optical Instrumentation Engineers (SPIE) Conference Series*, volume 8444 of *Society of Photo-Optical Instrumentation Engineers (SPIE) Conference Series*, September 2012.

A. P. Moisés, A. Damineli, E. Figuerêdo, R. D. Blum, P. S. Conti, and C. L. Barbosa. Spectrophotometric distances to Galactic H II regions. *MNRAS*, 411:705–760, February 2011.

S. Molinari, J. Brand, R. Cesaroni, F. Palla, and G. G. C. Palumbo. A search for precursors of ultracompact H II regions in a sample of luminous IRAS sources. II. VLA observations. *A&A*, 336:339–351, August 1998.

J. D. Monnier, T. R. Geballe, and W. C. Danchi. Temporal Variations of Midinfrared Spectra in Late-Type Stars. *ApJ*, 502:833–846, August 1998.

T. Nakamura. *30-micron imaging and analysis of circumstellar dust around Luminous Blue Variables*. PhD thesis, Institute of Astronomy, School of science, the University of Tokyo, Tokyo, Japan, December 2011.

T. Nakamura, T. Miyata, S. Sako, K. Asano, M. Uchiyama, T. Tanabe, M. Yoneda, Y. Ita, T. Onaka, H. Kataza, T. Aoki, M. Doi, T. Handa, D. Kato, K. Kawara, K. Kohno, M. Konishi, S. Koshida, T. Minezaki, N. Mitani, K. Motohara, R. Ohsawa, T. Soyano, M. Tanaka, K. Tarusawa, K. Toshikawa, and Y. Yoshii. MiniTAO/MAX38 first light: 30-micron band observations from the ground-based telescope. In *Society of Photo-Optical Instrumentation Engineers (SPIE) Conference Series*, volume 7735 of *Society of Photo-Optical Instrumentation Engineers (SPIE) Conference Series*, July 2010.

P. Padoan and Å. Nordlund. The Stellar Initial Mass Function from Turbulent Fragmentation. *ApJ*, 576:870–879, September 2002.

F. Palla and S. W. Stahler. The Pre-Main-Sequence Evolution of Intermediate-Mass Stars. *ApJ*, 418:414, November 1993.

J. P. Phillips. Constraints upon density gradients in evolved HII regions. *New A*, 13:60–64, January 2008.

A. Pietrinferni, S. Cassisi, M. Salaris, and F. Castelli. A Large Stellar Evolution Database for Population Synthesis Studies. I. Scaled Solar Models and Isochrones. *ApJ*, 612:168–190, September 2004.

J. A. Rodon. *The Fragmentation of Massive Star-Forming Regions*. PhD thesis, Max-Planck-Institut fur Astronomie, Heidelberg, Germany, November 2009.

E. E. Salpeter. The Luminosity Function and Stellar Evolution. *ApJ*, 121:161, January 1955.

N. Z. Scoville and J. Kwan. Infrared sources in molecular clouds. *ApJ*, 206:718–727, June 1976.

L. Siess, E. Dufour, and M. Forestini. An internet server for pre-main sequence tracks of low- and intermediate-mass stars. *A&A*, 358:593–599, June 2000.

M. Simon, L. Cassar, M. Felli, J. Fischer, M. Massi, and D. Sanders. Star formation in the M8E region. *ApJ*, 278:170–175, March 1984.

B. J. Smith. Infrared Colors and Variability of Evolved Stars from COBE DIRBE Data. *AJ*, 126:935–963, August 2003.

T. K. Sridharan, H. Beuther, P. Schilke, K. M. Menten, and F. Wyrowski. High-Mass Protostellar Candidates. I. The Sample and Initial Results. *ApJ*, 566:931–944, February 2002.

J. C. Tan, M. T. Beltrán, P. Caselli, F. Fontani, A. Fuente, M. R. Krumholz, C. F. McKee, and A. Stolte. Massive Star Formation. *Protostars and Planets VI*, pages 149–172, 2014.

R. I. Thompson. Lyman and Balmer continuum ionization in zero-age main-sequence stas - Applications to the line excess phenomenon. *ApJ*, 283:165–168, August 1984.

N. F. H. Tothill, G. J. White, H. E. Matthews, W. H. McCutcheon, M. J. McCaughrean, and M. A. Kenworthy. The Structure and Evolution of the Lagoon Nebula. I. Submillimeter Continuum and CO Line Mapping. *ApJ*, 580:285–304, November 2002.

J. S. Urquhart, A. L. Busfield, M. G. Hoare, S. L. Lumsden, R. D. Oudmaijer, T. J. T. Moore, A. G. Gibb, C. R. Purcell, M. G. Burton, L. J. L. Maréchal, Z. Jiang, and M. Wang. The RMS survey. ^{13}CO observations of candidate massive YSOs in the northern Galactic plane. *A&A*, 487:253–264, August 2008a.

J. S. Urquhart, M. G. Hoare, S. L. Lumsden, R. D. Oudmaijer, and T. J. T. Moore. The RMS Survey: A Galaxy-wide Sample of Massive Young Stellar Objects. In H. Beuther, H. Linz, and T. Henning, editors, *Massive Star Formation: Observations Confront Theory*, volume 387 of *Astronomical Society of the Pacific Conference Series*, page 381, May 2008b.

J. S. Urquhart, M. G. Hoare, C. R. Purcell, S. L. Lumsden, R. D. Oudmaijer, T. J. T. Moore, A. L. Busfield, J. C. Mottram, and B. Davies. The RMS survey. 6 cm continuum VLA observations towards candidate massive YSOs in the northern hemisphere. *A&A*, 501:539–551, July 2009.

A. J. Walsh, M. G. Burton, A. R. Hyland, and G. Robinson. Studies of ultracompact HII regions - II. High-resolution radio continuum and methanol maser survey. *MNRAS*, 301:640–698, December 1998.

J. L. Weiland, N. Odegard, R. S. Hill, E. Wollack, G. Hinshaw, M. R. Greason, N. Jarosik, L. Page, C. L. Bennett, J. Dunkley, B. Gold, M. Halpern, A. Kogut, E. Komatsu, D. Larson, M. Limon, S. S. Meyer, M. R. Nolta, K. M. Smith, D. N. Spergel, G. S. Tucker, and E. L. Wright. Seven-year Wilkinson Microwave Anisotropy Probe (WMAP) Observations: Planets and Celestial Calibration Sources. *ApJS*, 192:19, February 2011.

Y. Yoshii, T. Aoki, M. Doi, T. Handa, K. Kawara, D. Kato, K. Kohno, M. Konishi, S. Koshida, T. Minezaki, N. Mitani, T. Miyata, K. Motohara, S. Sako, T. Soyano, T. Tanabe, M. Tanaka, K. Tarusawa, L. Bronfman, M. T. Ruiz, and M. Hamuy. The University of Tokyo Atacama Observatory 6.5m telescope project. In *Society of Photo-Optical Instrumentation Engineers (SPIE) Conference Series*, volume 7733 of *Society of Photo-Optical Instrumentation Engineers (SPIE) Conference Series*, July 2010.

Y. Yoshii, M. Doi, K. Kohno, T. Miyata, K. Motohara, K. Kawara, M. Tanaka, T. Minezaki, S. Sako, T. Morokuma, Y. Tamura, T. Tanabe, H. Takahashi, M. Konishi, T. Kamizuka, S. Koshida, N. Kato, T. Aoki, T. Soyano, K. Tarusawa, T. Handa, L. Bronfman, M. T. Ruiz, M. Hamuy, and R. Mendez. Overview of University of Tokyo Atacama Observatory 6.5m telescope project. In *Society of Photo-Optical Instrumentation Engineers (SPIE) Conference Series*, volume 9145 of *Society of Photo-Optical Instrumentation Engineers (SPIE) Conference Series*, page 7, July 2014.

H. Zinnecker and H. W. Yorke. Toward Understanding Massive Star Formation. *ARA&A*, 45: 481–563, September 2007.